Journal of
METAMORPHIC GEOLOGY

J. metamorphic Geol., 2013 doi:10.1111/jmg.12050

Quantifying Barrovian metamorphism in the Danba Structural Culmination of eastern Tibet

O. M. WELLER,[1] M. R. ST-ONGE,[2] D. J. WATERS,[1] N. RAYNER,[2] M. P. SEARLE,[1] S.-L. CHUNG,[3] R. M. PALIN,[1] Y.-H. LEE[4] AND X. XU[5]
[1]Department of Earth Sciences, University of Oxford, South Parks Road, Oxford, OX1 3AN, UK (owen.weller@earth.ox.ac.uk)
[2]Geological Survey of Canada, 601 Booth Street, Ottawa, Ontario, K1A 0E8, Canada
[3]Department of Geosciences, National Taiwan University (NTU), Taipei, 106, Taiwan
[4]Department of Earth and Environmental Sciences, National Chung-Cheng University, Minxueng, Taiwan
[5]Institute of Geology, China Earthquake Administration (CEA), Beijing, 100029, China

ABSTRACT The Danba Structural Culmination is a tectonic window into the late Triassic to early Jurassic Songpan-Garzê Fold Belt of eastern Tibet, which exposes an oblique section through a complete Barrovian-type metamorphic sequence. Systematic analysis of a suite of metapelites from this locality has enabled a general study of Barrovian metamorphism, and provided new insights into the early thermotectonic history of the Tibetan plateau. The suite was used to create a detailed petrographic framework, from which four samples ranging from staurolite to sillimanite grade were selected for thermobarometry and geochronology. Pseudosection analysis was applied to calculate *P–T* path segments and determine peak conditions between staurolite grade at ~5.2 kbar and 580 °C and sillimanite grade at ~6.0 kbar and 670 °C. *In situ* U–Pb monazite geochronology reveals that staurolite-grade conditions were reached at 191.5 ± 2.4 Ma, kyanite-grade conditions were attained at 184.2 ± 1.5 Ma, and sillimanite-grade conditions continued until 179.4 ± 1.6 Ma. Integration of the results has provided constraints on the evolution of metamorphism in the region, including a partial reconstruction of the regional metamorphic field gradient. Several key features of Barrovian metamorphism are documented, including nested *P–T* paths and a polychronic field gradient. In addition, several atypical features are noted, such as *P–T* path segments having similar slopes to the metamorphic field gradient, and T_{max} and P_{max} being reached simultaneously in some samples. These features are attributed to the effects of slow tectonic burial, which allows for thermal relaxation during compression. While nested, clockwise *P–T–t* loops provide a useful framework for Barrovian metamorphism, this study shows that the effects of slow burial can telescope this model in *P–T* space. Finally, the study demonstrates that eastern Tibet experienced a significant phase of crustal thickening during the Mesozoic, reinforcing the notion that the plateau may have a long history of uplift and growth.

Key words: Barrovian metamorphism; metamorphic field gradient; *in situ* monazite geochronology; *P–T–t* path; Tibetan plateau.

INTRODUCTION

It was the British geologist George Barrow who first documented a sequence of mineral zones—chlorite, biotite, garnet, staurolite, kyanite and sillimanite—associated with the progressive metamorphism of mudstone in the late 19th century (Barrow *et al.*, 1893, 1912). This sequence has since been observed in numerous orogenic belts, and Barrovian metamorphism has become synonymous with continental collision (e.g. England & Thompson, 1984). Thermal modelling of collisional belts has greatly developed our understanding of Barrovian metamorphism, by demonstrating how plausible burial, internal heating and erosion rates can produce clockwise pressure–temperature–time (*P–T–t*) loops that traverse documented *P–T* conditions (e.g. England & Richardson, 1977; Jamieson *et al.*, 1998). Advances in thermobarometry and geochronology are now furthering our knowledge, as nuanced *P–T–t* paths can be extracted from natural settings and compared with theoretical models (e.g. Gerya & Maresch, 2004).

In this contribution, the Danba Structural Culmination (DSC) in the Songpan-Garzê Fold Belt of eastern Tibet (Fig. 1) was used as a natural case study of Barrovian metamorphism. The DSC is well suited for this purpose, because it exposes a complete Barrovian sequence within a small geographical area, with high-quality outcrops and a well-established regional context (Huang *et al.*, 2003a; Roger *et al.*, 2010). Integrated pseudosection modelling and *in situ* monazite geochronology were applied to a suite of

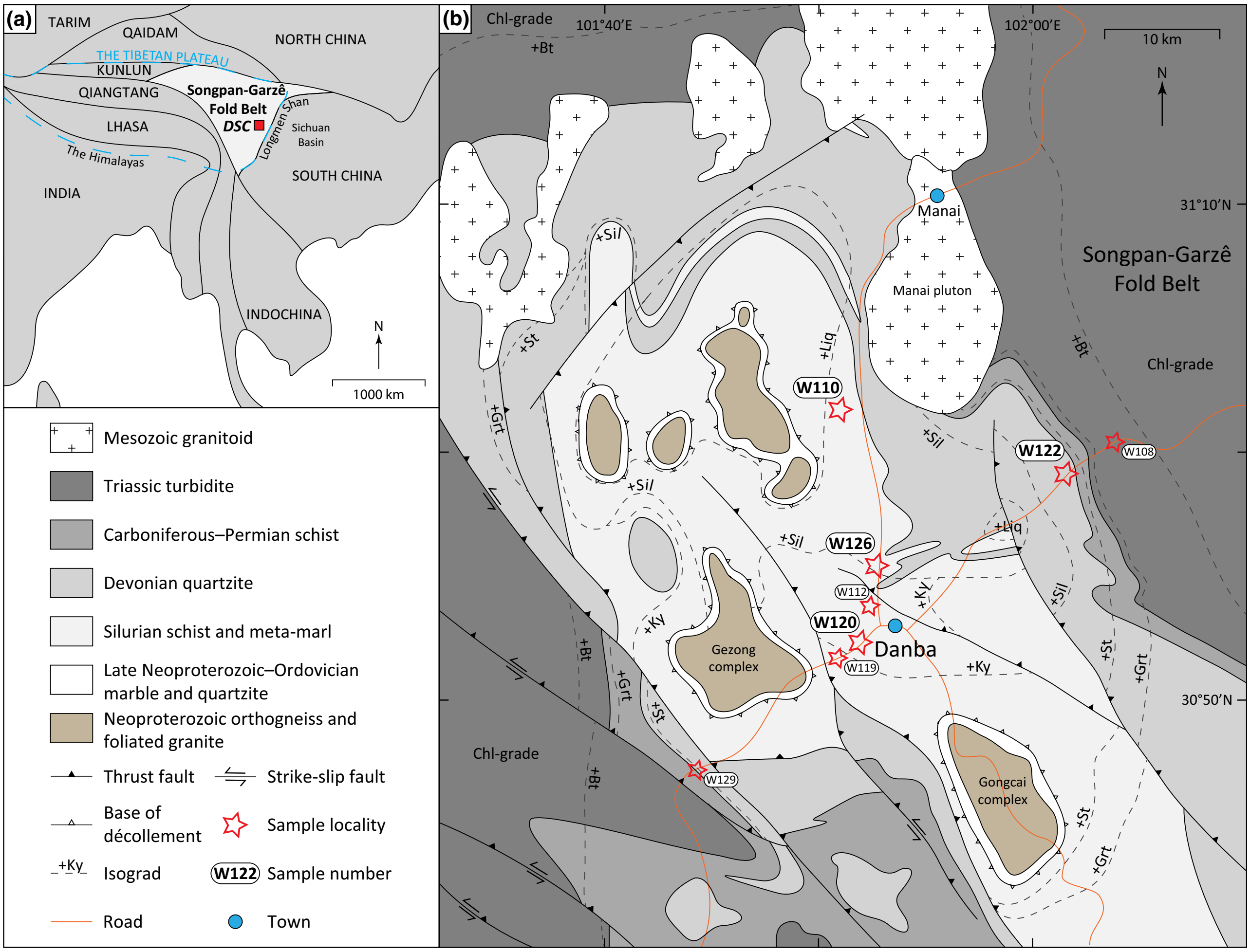

Fig. 1. Field setting. (a) Tectonic block map of Asia. The location of the Danba Structural Culmination (DSC) within the Songpan-Garzê Fold Belt is shown by the red box. Modified from Roger *et al.* (2010). (b) Geological map showing the stratigraphy and metamorphic isograds of the DSC. All samples are used to develop the petrographic framework; the four large red stars denote the samples used for thermobarometry and geochronology. Modified from Huang *et al.* (2003a).

metapelites from the DSC, to quantify the petrological, thermobarometric, and temporal evolution of metamorphism in the region. The aim was to explore a series of *P–T–t* paths from different metamorphic grades, for comparison with the classic model of nested, clockwise *P–T–t* loops (Fig. 2; England & Richardson, 1977). This included consideration of the metamorphic field gradient, which is defined as the *P–T* loci of T_{max} for rocks from all exposed structural levels (Richardson & England, 1979; Thompson & England, 1984; Spear, 1993).

This study is also of regional relevance because the DSC represents one of the few tectonic windows into the Tibetan plateau, providing a direct means to access the crustal history of Tibet and evaluate geodynamic models of how and when the plateau formed (Clark, 2011). At present, this approach is hampered in the DSC by conflicting ages and interpretations pertaining to whether the sillimanite-grade metamorphism was an integral part of the early Jurassic metamorphism, or a separate thermal event (Mattauer *et al.*, 1992; Huang *et al.*, 2003b; Wallis *et al.*, 2003). Our results support a model of continuous prograde metamorphism in the study area, with the implications for Barrovian metamorphism and the crustal evolution of the Tibetan plateau discussed below.

GEOLOGICAL SETTING

Songpan-Garzê Fold Belt

The Songpan-Garzê Fold Belt is a triangular-shaped terrane situated in the eastern part of the Tibetan plateau (Fig. 1a; Roger *et al.*, 2008). It was formed during inversion of a large sedimentary basin in the late Triassic, due to concurrent convergence between the North China, South China and Qiangtang blocks.

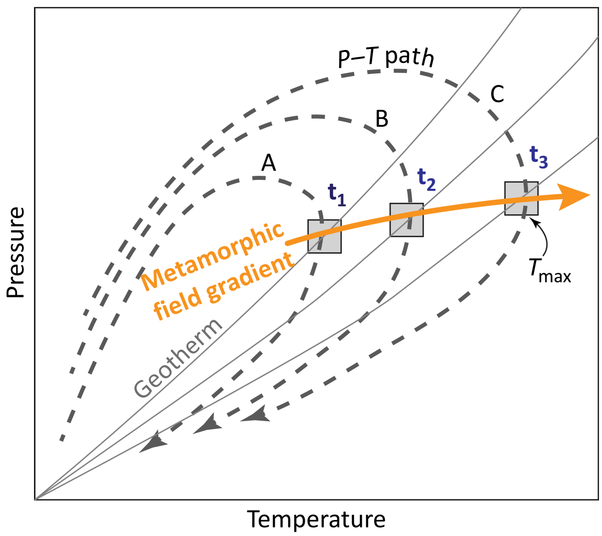

Fig. 2. Schematic showing a cogenetic suite of P–T–t paths for three samples (A, B & C) involved in crustal thickening. The P–T loci of their respective T_{max} positions define the metamorphic field gradient, which is typically concave to the T-axis, polychronic and at a steep angle to the P–T paths of an individual sample (England & Richardson, 1977; Richardson & England, 1979; Thompson & England, 1984; Spear, 1993).

The northern and western boundaries of the Songpan-Garzê Fold Belt are northward- and eastward-dipping Triassic subduction zones, respectively (Dewey *et al.*, 1988). The eastern boundary is the transpressive, polyphase Triassic–Tertiary Longmen Shan fold-and-thrust belt, which also forms the topographic edge to the Tibetan plateau and separates the Songpan-Garzê Fold Belt from the Sichuan Basin below (Burchfiel *et al.*, 1995).

The Songpan-Garzê basin comprised a 6–8 km deep Triassic infill of turbidite, which was deposited on a 5–7 km thick late Neoproterozoic–Palaeozoic sequence underlain by a Neoproterozoic crystalline basement (Zhou *et al.*, 2002). Shortening across the basin caused the development of a NW-trending, SW-verging, regional décollement-fold belt (the Songpan-Garzê Fold Belt), which induced amphibolite facies, Barrovian-type metamorphism in the thickened sedimentary pile (Huang *et al.*, 2003a). From exposed higher to lower structural levels, the deformation style changes from upright chevron folding of Triassic strata, with a variably developed axial-planar slaty cleavage, to a flat-lying, isoclinally folded ductile décollement zone primarily located in Silurian–Devonian strata, with a penetrative axial-planar foliation (Mattauer *et al.*, 1992; Harrowfield & Wilson, 2005). The décollement zone is associated with a north-south stretching lineation, with shear criteria indicating a top-to-the-south sense of shear.

Granitic magmatism is extensive in the region, with more than one hundred plutons intruding the Songpan-Garzê Fold Belt, ranging in age from *c.* 225 to *c.* 150 Ma. The older granites (*c.* 225–190 Ma) are interpreted to have resulted from partial melting of the basement, and are pre- to syn-kinematic with respect to formation of the Songpan-Garzê Fold Belt, whereas the younger granites are suggested to be post-orogenic and derived from partial melting of the thickened sedimentary cover sequence (Roger *et al.*, 2004).

The Songpan-Garzê Fold Belt largely retains its Triassic architecture, with extremely slow cooling (<1 °C Ma^{-1}) and very little denudation and exhumation since the Jurassic (Kirby *et al.*, 2002). Tertiary deformation in the region is restricted to two fault systems. First, a suite of large sinistral strike-slip faults, associated with the lateral extrusion of the Tibetan plateau, have developed in the southern part of the Songpan-Garzê Fold Belt since the mid-Miocene (Roger *et al.*, 1995). Second, the Longmen Shan has been reactivated, most notably during the 2008 Wenchuan earthquake, and has experienced rapid denudation since the late Miocene (Xu & Kamp, 2000; Xu *et al.*, 2009). Consequently, most of the Songpan-Garzê Fold Belt outcrops in its upper structural levels, with basement sections only exposed in the Longmen Shan and the DSC (Fig. 1a; Roger *et al.*, 2010).

Danba Structural Culmination

The DSC is a wide, Tertiary, NNW-plunging antiformal culmination, which exposes the lower structural levels of the Songpan-Garzê Fold Belt (Fig. 1b; Burchfiel *et al.*, 1995). Within the DSC, a series of basement-cored structural domes consist of Neoproterozoic orthogneiss and foliated granite that are locally reworked near the décollement horizon (Zhou *et al.*, 2002). Igneous components within two of the basement domes, the Gongcai and Gezong complexes, have been dated at 824 ± 14 Ma and 864 ± 8 Ma, respectively (U–Pb zircon; Zhou *et al.*, 2002). The cover sequence comprises a lowermost marble unit with subordinate quartzite, which is overlain by Silurian–Devonian schist, meta-marl and quartzite, interlayered with minor amphibolite. Carboniferous–Permian schist and Triassic turbidite form the upper part of the sequence (Mattauer *et al.*, 1992).

Pelitic horizons are found throughout this sequence and isograd mapping documents a classic Barrovian sequence into the core of the DSC, which culminates in partial melting (Fig. 1b; Huang *et al.*, 2003a). However, there remains significant debate pertaining to whether the sillimanite-grade metamorphism (and associated anatexis) was progressive with the kyanite grade metamorphism during evolution of the Songpan-Garzê Fold Belt, or whether it represents a separate thermal event. This is fuelled by considerable scatter in published ages (see discussion below;

Hou *et al.*, 1996; Huang *et al.*, 2003b; Wallis *et al.*, 2003). Aluminosilicate-bearing quartz veins are also prevalent in the core of the DSC.

Previous metamorphic studies

Mattauer *et al.* (1992) suggested that all of the metamorphism in the DSC was contemporaneous with formation of the Songpan-Garzê Fold Belt. Wallis *et al.* (2003) made the same interpretation, noting that all of the metamorphic minerals, including sillimanite, define a similar foliation. However, Huang *et al.* (2003a) distinguished an initial M_1 Barrovian metamorphism, peaking at kyanite-grade conditions of 5.3–8 kbar and 570–600 °C, from a sillimanite-grade overprint (M_2), which was suggested to have occurred only in the northern part of the DSC (marked by the occurrence of sillimanite and local migmatization) at *P–T* conditions of 4.8–6.3 kbar and 640–725 °C. Huang *et al.* (2003a) primarily used the avPT method of THERMOCALC for their thermobarometric calculations (Powell & Holland, 1994). Cheng & Lai (2005) applied conventional thermobarometry to samples located across the DSC, and concluded that Barrovian metamorphism occurred at moderate pressures, with results ranging between 3.1–6.3 kbar and 430–660 °C. Their data also show *P–T* paths that are consistently clockwise, and a variable geotherm, in the range 23–55 °C km^{-1}. They also noted that sillimanite and migmatite lenses align with the regional foliation. Lastly, Cheng *et al.* (2009) presented an analysis of a single, compositionally zoned, poikiloblastic garnet from a kyanite-sillimanite-schist from the DSC, and calculated an anticlockwise *P–T* growth trajectory from $\sim$4.9 kbar and 540 °C at the core to $\sim$5.8 kbar and 530 °C at the rim. However, the Gibbs method applied by Cheng *et al.* (2009) requires that no diffusional modification of the sillimanite-grade garnet core had occurred, and contradicts the results presented in Cheng & Lai (2005).

Previous geochronological studies

Hou *et al.* (1996) obtained whole rock Rb–Sr mineral isochron ages of 160–150 Ma for a kyanite-schist and an amphibolite from the DSC, which they interpreted to approximate the timing of kyanite-grade metamorphism in the region. Huang *et al.* (2003b) used an array of techniques (U–Pb monazite, U–Pb titanite and Sm–Nd garnet) to analyse the high-temperature geochronology of the region. They dated M_1 (as defined above for Huang *et al.*, 2003a) at *c.* 204–190 Ma, and concluded that M_2 was a separate thermal event that only affected the northern part of the Danba terrane at 165–158 Ma. All of their datasets show considerable dispersion from *c.* 200 to *c.* 160 Ma, which Huang *et al.* (2003b) attributed to variable recrystallization of older monazite during the M_2 overprint. They also reported Rb–Sr muscovite ages of *c.* 138–100 Ma and Rb–Sr biotite ages of *c.* 34–24 Ma. Wallis *et al.* (2003) suggested an age of *c.* 65 Ma for sillimanite-grade metamorphism in the DSC, based on similar ages from two different methods: 65 ± 3 Ma for the chemical Th–U total lead isochron method (CHIME) dating of monazite from a sillimanite-bearing schist, and 67 ± 12 Ma for U–Pb dating of apatite from the Manai pluton. However, the Manai pluton has since been dated by U–Pb zircon at 197 ± 6 Ma (Roger *et al.*, 2004), so that the 65 ± 3 Ma CHIME age determination is considered as yet non-reproduced. Lastly, Tung *et al.* (2011) used an array of low-temperature techniques to focus on the exhumation history of the DSC, with biotite Rb–Sr ages of 34–24 Ma, zircon fission track ages of 25–19 Ma at the margin and 14–16 Ma at the core of DSC, and apatite fission track ages of 12–9 Ma at the margin and 7–5 Ma at the core of DSC. Their results suggest that the folding associated with the formation of the DSC has been ongoing since the Miocene.

PETROGRAPHY

Sampling strategy

Samples of metapelite were collected from each mineral zone in the DSC (red stars, Fig. 1b), allowing fabric development and mineral growth to be tracked across the full width of the Barrovian sequence. Using this framework, a subset of four study samples (W122, W120, W126 & W110; Fig. 1b) were chosen for systematic application of pseudosection modelling and *in situ* monazite geochronology. The study samples represent a prograde sequence with peak assemblages characterized by staurolite (W122), kyanite (W120), kyanite-sillimanite (W126) and sillimanite (W110). A staurolite-grade sample provides the lower temperature bound because monazite was only observed to be present from staurolite grade onwards (Table 1). All mineral abbreviations follow the guidelines given in Whitney & Evans (2010).

Fabric development in the DSC

The DSC exposes a continuous section from chlorite-grade sedimentary rocks on the flanks of the DSC, to sillimanite-grade migmatites in the core, which allows for progressive fabric development to be monitored relative to S_0. Figure 3a,b shows the characteristic mesoscopic S_0–S_1 relations of the Songpan-Garzê Fold Belt, with a fold-axial-planar slaty cleavage (S_1) developed within tight upright folds (F_1) in response to shortening across the Songpan-Gârze basin (D_1). The S_1 foliation contains a stretching lineation (L_1), which is manifested by alignment of disaggregated pyrite at lower grades (Fig. 3c), and by preferential growth direction of kyanite and sillimanite at higher grades. Field shear criteria and sections cut parallel the stretching lineation consistently show a top-to-

Table 1. X-ray fluorescence data (wt%) for all samples, sorted by grade.

Sample	Grade	SiO_2	TiO_2	Al_2O_3	Fe_2O_3	MnO	MgO	CaO	Na_2O	K_2O	P_2O_5	LOI	Total	Aln or Mnz
W108	Bt	59.19	0.62	15.63	6.37	0.10	3.14	6.30	1.47	2.98	0.13	3.76	99.70	Aln
W129	Grt-St	60.50	0.78	19.33	7.26	0.04	3.15	0.44	0.43	5.17	0.07	2.47	99.64	Aln
W122	St	54.70	1.01	23.06	9.33	0.09	3.49	0.60	1.04	4.25	0.09	1.94	99.61	Aln + Mnz
W119	St	59.66	0.74	19.54	7.65	0.08	3.23	0.19	0.63	4.95	0.09	2.90	99.66	Aln + Mnz
W120	Ky	61.84	0.70	18.51	7.70	0.10	3.15	0.39	0.81	4.53	0.06	1.81	99.60	Mnz
W112	Ky	56.59	0.96	22.74	7.59	0.07	3.23	0.31	0.82	4.93	0.12	2.25	99.63	Mnz
W126	Ky-Sil	62.87	0.67	17.75	6.53	0.07	2.78	0.95	1.88	3.71	0.10	2.30	99.61	Mnz
W110	Sil	58.79	1.02	20.11	8.16	0.07	3.55	0.29	0.63	5.15	0.08	1.75	99.60	Mnz

the-south sense of shear. This orientation is concordant with previous studies in the DSC, and is considered to represent the transport direction of the Songpan-Garzê Fold Belt (Huang *et al*., 2003a; Wallis *et al*., 2003; Harrowfield & Wilson, 2005).

Figure 3d shows the corresponding microscopic S_0–S_1 relations at biotite grade, with an incipient slaty cleavage (S_1) developing axial-planar to microfolds of S_0. Above garnet grade, deformation intensifies and S_1 becomes the dominant planar fabric observed within the metasedimentary rocks in the DSC. In finer-grained samples, the S_1 cleavage is penetrative, but characteristically it is spaced at 0.5–1 mm intervals, with well-defined alternating cleavage and microlithon domains (Fig. 3e). Evidence for S_0 becomes scarce due to realignment of mica into S_1 and extensive recrystallization. However, extrapolation of the S_0–S_1 microstructural framework up grade is permissible by the observation of relict S_0 microfolding within local strain shadows in sections where S_1 is otherwise well developed, e.g. within the arms of a staurolite cruciform twin (Fig. 3f,g).

In the centre of the DSC, an incipient, sub-vertical S_2 crenulation cleavage is developed. In general, S_2 is associated with mild crenulation of S_1 along a N–S axis (L_2), and is interpreted to result from E–W compression (D_2). D_2 overprints all index minerals, and is associated with microstructures indicative of relatively low temperatures, such as kink banding of mica (Fig. 3h) and bulging recrystallization in quartz (Fig. 3i). The latter has been calibrated by Stipp *et al*. (2002) to indicate temperatures of deformation between 280–400 °C, which suggests that D_2 was a relatively late feature of the DSC.

Mineral growth and stability in the DSC

The graphitic nature of the pelitic samples utilized in this study provides a common textural context within which the progressive nature of mineral growth across a range of metamorphic grades can be documented.

Barrovian minerals

Chlorite is well developed along the flanks of the DSC, occurring as small flakes throughout the matrix. Biotite is the first index mineral to appear within the DSC, forming large poikiloblasts that commonly overgrow F_1 microfolds (Fig. 4a). At higher grade, biotite porphyroblasts are truncated and realigned into the dominant S_1 fabric (Fig. 3e). Taken as a set, these observations suggest that biotite grew after the onset of D_1, but that deformation outlasted mineral growth (Passchier & Trouw, 2005). This lends a characteristic fabric element to all higher-grade samples: truncated biotite porphyroblasts that define the limits of the S_1 microlithon domains. Garnet, which is the second index mineral that characterizes the DSC, forms large poikiloblasts that are wrapped by S_1 and contain S-shaped inclusions trails, dominantly of aligned quartz grains, which are continuous with the external fabric, suggesting that garnet grew syn-D_1 (Fig. 4b; Passchier & Trouw, 2005). The same observations for garnet hold at staurolite grade, and staurolite poikiloblasts are also observed to be wrapped by S_1 and contain curved inclusion trails, consistent with syn-D_1 growth (Fig. 3f).

Staurolite breakdown is coincident with kyanite growth (Fig. 4c), with kyanite typically forming blades that are aligned within S_1 (Fig. 4d,g). Although alignment within a fabric is not in itself definitive, the observation of syn-D_1 garnet and staurolite growth suggests that kyanite also grew syn-D_1. The kyanite-bearing S_1 fabric is deflected around inclusion-rich garnet cores, but is in turn overgrown by thin, inclusion-poor garnet rims (rounded black box, Fig. 4d), suggesting that the garnet rims grew post-D_1. Similar aluminosilicate-garnet-matrix relations are observed at sillimanite grade, where sillimanite is aligned within the S_1 fabric that is deflected around garnet cores, but is truncated by thin garnet rims that overgrow S_1 (Fig. 4e). The inclusion-poor rims are wider at higher grades (Fig. 4f), but only partially overgrow S_1 at their outer margins. Analysis of garnet compositional zonation below shows that the microstructurally defined post-D_1 garnet rims are also chemically distinctive.

Where kyanite and sillimanite coexist, sillimanite typically nucleates in muscovite, away from resorbed kyanite blades (Fig. 4h). This texture is typical of the kyanite-sillimanite transition in the DSC and is interpreted to be the result of the sluggish reaction kinetics associated with polymorphic replacement

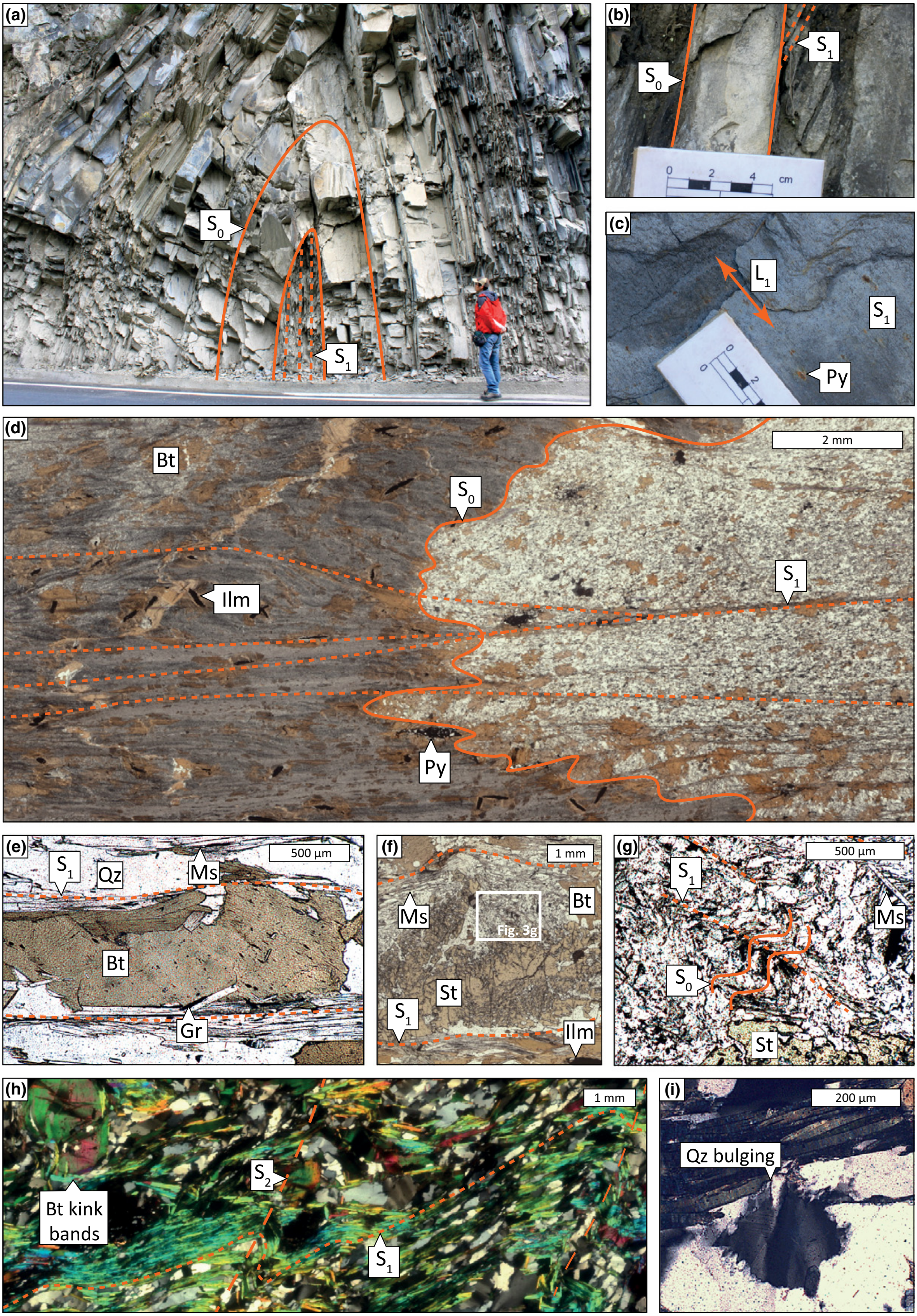
(a)
S0
S1
(b)
S0
S1
0 2 4 cm
(c)
L1
S1
Py
(d)
2 mm
Bt
S0
Ilm
S1
Py
(e)
500 µm
S1
Qz
Ms
Bt
Gr
(f)
1 mm
Ms
Bt
Fig. 3g
St
S1
Ilm
(g)
500 µm
S1
Ms
S0
St
(h)
1 mm
S2
Bt kink bands
S1
(i)
200 µm
Qz bulging

(Carmichael, 1969). Fibrolite mats and sillimanite blades also show strong alignment within S_1, and in places define the spaced S_1 cleavage (Fig. 4i), which is consistent with syn-D_1 growth. At sillimanite grade, garnet is ragged in appearance, suggestive of resorption. Finally, migmatitic samples are observed to have quartzofeldspathic lenses aligned with S_1, but they are not mentioned further in this paper as their analysis is beyond the scope of this study.

Other minerals

In all samples, quartz, plagioclase and ilmenite are found as major phases, and graphite, tourmaline, zircon and apatite are accessory phases. Allanite is present in low-grade samples, typically rimmed by epidote, but is replaced by monazite from staurolite grade onwards (Table 1). Calcite and pyrite are also present at biotite grade. Most of the samples display little indication of retrogression, except for some minor late muscovite, which form blades that randomly cut across the S_1 cleavage. The exception to this are samples that contain S_2 fabrics, which show evidence of retrograde chlorite growth along the S_2 planes, with shimmer aggregates after staurolite and conversion of matrix mica to chlorite. This suggests that D_2 enabled localized retrogressive fluid flow.

Coarse-grained aluminosilicate-bearing quartz veins are present in the core of the DSC, and are variably, but not always completely, discordant with S_1, suggesting late- to post-D_1 emplacement. The aluminosilicate polymorph is the same in both the vein and matrix assemblage and the veins are interpreted to be derived from prograde dehydration reactions in the adjacent host metapelite (Allaz *et al.*, 2005).

Petrographic summary

Figure 5 summarizes the interpretation of fabric development *v.* mineral growth for all major mineral phases in the DSC. The key observation is that all of the index minerals are aligned within or wrapped by S_1, which suggests that Barrovian metamorphism in the DSC occurred entirely within a progressive D_1 event.

MINERAL CHEMISTRY

Analytical techniques

Whole-rock major element data were acquired for all samples using XRF techniques on fused glass beads using a Rigaku® RIX-2000 spectrometer at the Department of Geosciences, National Taiwan University. The analytical procedures follow Wang (2004), yielding analytical uncertainties generally better than ±5% (2σ). Loss on ignition (LOI) was determined separately by routine procedures. Mineral compositional data (point analyses of individual minerals and compositional line profiles traversing garnet porphyroblasts) were acquired for each of the four study samples (W122, W120, W126 & W110) using a JEOL JSM-840A scanning electron microscope (SEM) fitted with an Oxford Instruments Isis 300 energy-dispersive analytical system at the Department of Earth Sciences, University of Oxford. Accelerating voltage was 20 kV, with a beam current of 6 nA, and a live counting time of 100. It was calibrated with a range of natural and synthetic standards, and a ZAF correction procedure was used. The beam current was checked regularly and the count rate calibrated every 120 min using a cobalt metal standard. Compositional profiles across garnet were determined by accumulating counts along a 256-channel line scan for ~30 min. The profiles were background-corrected and calibrated against up to six full point analyses taken at known positions along the profile to calculate mole factions of garnet end members. By convention, all Fe is reported as ferric (Fe^{3+}) in XRF analyses, but conversely, all Fe is reported as ferrous (Fe^{2+}) in SEM analyses.

Sample chemistry

Table 1 displays the whole-rock major element XRF data for all samples. Alongside Table 1, a summary of whether allanite and/or monazite was present in each sample is given, which shows that monazite replaces allanite within staurolite-grade samples. Tables 2 & 3 contain representative compositional SEM analyses for suitable minerals within each of the four study samples (W122, W120, W126 & W110). The analyses are presented as the average of

Fig. 3. Fabric development in the DSC. All photomicrographs are from sections cut normal to S_1 and parallel L_1, unless otherwise stated. (a) Field photograph taken to the east of the DSC, showing a typical view of the upper structural levels of the Songpan-Garzê Fold Belt and comprising folded Triassic turbidites with axial-planar cleavage (S_1). (b) Field photograph taken to the east of the DSC, showing S_0–S_1 intersection (F_1). (c) Field photograph taken near sample W108, showing the alignment of pyrite along the L_1 stretching lineation. (d) Plane-polarized light (PPL) photomicrograph of sample W108, showing S_1 axial-planar to microfolds of S_0. The competency difference between the sandstone and mudstone causes fanning of the S_1 cleavage. (e) PPL photomicrograph of sample W120, showing a biotite porphyroblast that is truncated by the spaced S_1 cleavage. (f) PPL photomicrograph of sample W122, showing a staurolite poikiloblast wrapped by S_1. (g) PPL photomicrograph of the boxed region in Fig. 3f, showing relict microfolding of S_0 in the strain shadow of the cruciform arms of the staurolite porphyroblast. (h) Photomicrograph of sample W119 viewed under crossed polars, showing the development of an incipient S_2 cleavage, from crenulation of S_1. Zones of S_2 deformation are associated with kink banding in mica. Section is cut normal to S_1 and perpendicular to L_1. (i) Close-up of Fig. 3h, showing characteristic quartz bulging microstructures that developed along S_2.

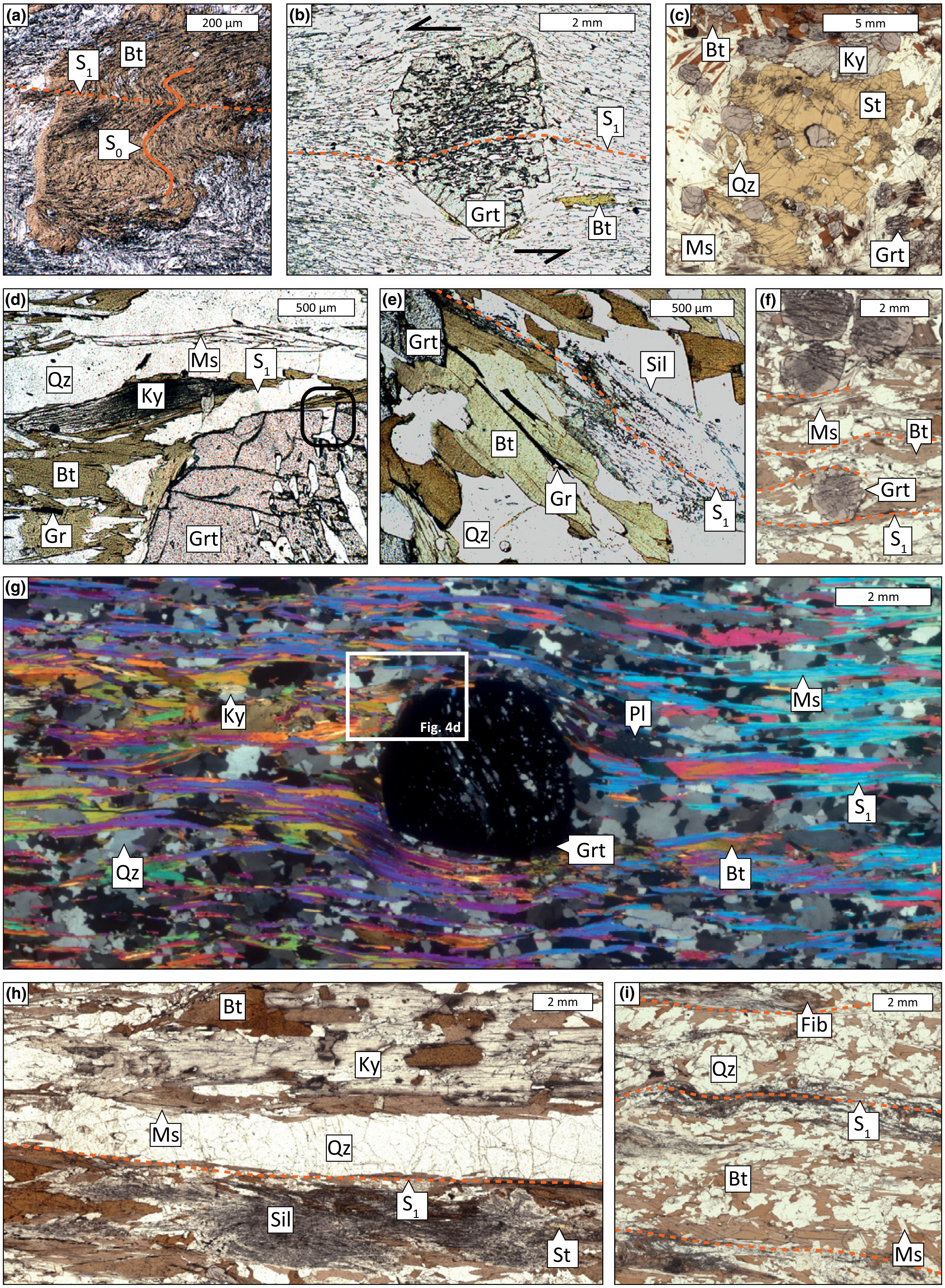
(a)
200 µm
S1
Bt
S0
(b)
2 mm
S1
Grt
Bt
(c)
5 mm
Bt
Ky
St
Qz
Ms
Grt
(d)
500 µm
Ms
S1
Qz
Ky
Bt
Gr
Grt
(e)
500 µm
Grt
Sil
Bt
Gr
Qz
S1
(f)
2 mm
Ms
Bt
Grt
S1
(g)
2 mm
Ky
Fig. 4d
Pl
Ms
S1
Qz
Grt
Bt
(h)
2 mm
Bt
Ky
Ms
Qz
S1
Sil
St
(i)
2 mm
Fib
Qz
S1
Bt
Ms

Fig. 4. Barrovian mineral growth in the DSC. All photomicrographs are from sections cut normal to S_1 and parallel L_1, unless otherwise stated. (a) PPL photomicrograph of sample W108, showing a biotite porphyroblast that is helicitic with respect to early microfolding of S_0. (b) PPL photomicrograph of sample W129, showing a garnet poikiloblast with an S-shaped inclusion trail that is continuous with S_1, indicative of syn-D_1 growth. The sense of shear is top-to-the-south. (c) PPL photomicrograph of sample W112, showing the breakdown of a large staurolite poikiloblast to kyanite, biotite and garnet. (d) PPL photomicrograph of the boxed region in Fig. 4g, showing detailed kyanite-garnet-S_1 relations. The matrix and garnet core are consistent with syn-D_1 growth, but the garnet rim overgrows the S_1 fabric (rounded black box), suggesting post-D_1 growth; see text for discussion. (e) PPL photomicrograph of sample W110, showing similar aluminosilicate-garnet-S_1 relations as for Fig. 4d, but for a sillimanite-grade sample. Sillimanite is strongly aligned within the S_1 fabric, consistent with syn-D_1 growth. (f) PPL photomicrograph of sample W126, showing inclusion-rich garnet cores and inclusion-poor garnet rims. The highly graphitic nature of this sample makes for a strong contrast. Section is cut normal to S_1 and perpendicular to L_1. (g) Photomicrograph of sample W120 viewed under crossed polars, showing the characteristic spaced S_1 cleavage. Kyanite blades are strongly aligned with S_1, consistent with syn-D_1 growth. (h) PPL photomicrograph of sample W126, showing resorbed kyanite blades and the nucleation of sillimanite in muscovite. Relict staurolite is also observed. (i) PPL photomicrograph of sample W110, showing sillimanite preferentially within the S_1 cleavage domains, suggestive of syn-D_1 growth. The characteristic spaced S_1 fabric is still clear, despite grain size coarsening.

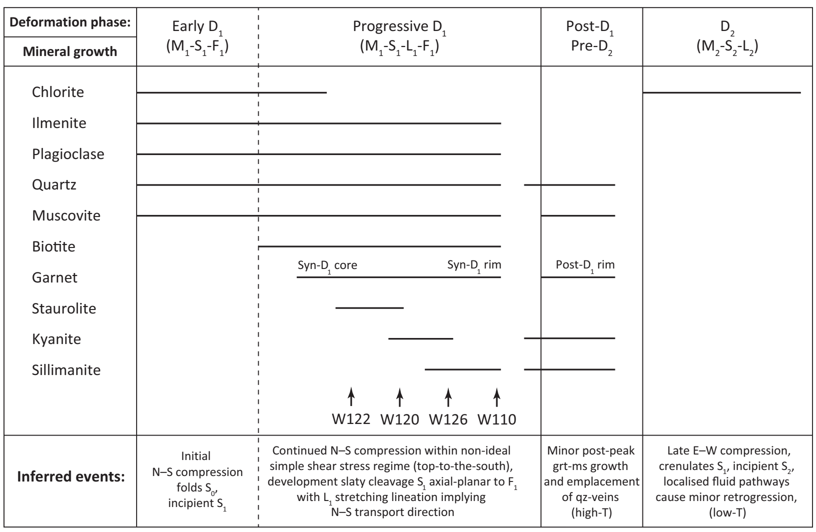

Fig. 5. Summary of fabric development *v.* mineral growth in the DSC. D_1 columns represent absolute assemblages in a closed system, whereas post-D_1 columns only show minerals that join the assemblages in an open system. Secondary garnet rims and late muscovite are grouped together based on the observation that they occurred in the absence of deformation and are assumed to be high temperature features, but they are not necessarily genetically associated. The major phase assemblage for each of the study samples (W122, W120, W126 & W110) is indicated by the arrows.

multiple grains, apart from the garnet columns, which represent individual analyses along the garnet profiles detailed below.

Garnet chemistry

Representative garnet compositional line profiles from each study sample are presented in Fig. 6a–d. Associated X-ray compositional maps for Mn content demonstrate that zoning is approximately concentric in all cases (Fig. 6e–h). The compositional profiles for samples W122 and W120 (Fig. 6a,b) have Mn- and Ca-rich cores, and Fe- and Mg-rich rims, which are typical trends for prograde garnet in metapelites (e.g. Woodsworth, 1977). Similar trends are observed for sample W126 (Fig. 6c), but the signal is more muted. The change in the nature of the garnet compositional zoning is particularly evident from the spessartine component (dark circles, Fig. 6a–d), which defines 'bell-shaped' prograde growth curves up to kyanite grade that become progressively flattened into the sillimanite zone. The flatter compositional profiles are interpreted to reflect increasing homogenization (by cation diffusion) at higher metamorphic grades (Tracy, 1982). Therefore, only core compositions up to kyanite grade are considered approximately primary.

Compositional trends at the rims are more complex, with a transition in behaviour between the staurolite-grade sample (W122), which shows an upward Mn inflexion in the rim region (Fig. 6a), and the higher grade samples, which all show a downward Mn inflexion (Fig. 6b–d), regardless of neighbouring mineral or relative homogenization of the garnet core chemistry. The upward inflexion is interpreted as minor resorption, as the Fe/(Fe+Mg) ratio is also observed to increase, whereas the downward inflexion is interpreted as secondary growth, given that Mn

Table 2. Representative mineral compositions for samples W122 and W120. X_{Mg} = Mg/(Mg + Fe^{2+}), Ti (22O) is the Ti content per 22 oxygen, Sps = Mn/(Fe^{2+} + Mg + Ca + Mn), Prp = Mg/(Fe^{2+} + Mg + Ca + Mn), Grs = Ca/(Fe^{2+} + Mg + Ca + Mn), Alm = Fe^{2+}/(Fe^{2+} + Mg + Ca + Mn)

Sample	W122 (St)							W120 (Ky)							
Mineral	Bt	Grt	Grt	Ilm	Ms	Pl	St	Bt	Grt	Grt	Grt	Ilm	Ms	Pl	St
Location	matrix	syn-D_1 core	syn-D_1 rim	matrix	matrix	matrix	matrix	matrix	syn-D_1 core	syn-D_1 rim	post-D_1 rim	matrix	matrix	matrix	matrix
Analyses	10	1	1	2	5	5	4	10	1	1	1	2	6	6	4
SiO_2	35.84	35.73	36.55	0.16	45.10	62.03	26.64	35.72	36.24	36.42	36.09	0.11	45.45	63.16	26.87
TiO_2	1.73	0.05	0.04	53.87	0.65	0.02	0.54	2.05	0.03	0.05	0.00	52.89	0.74	0.02	0.69
Al_2O_3	19.06	20.49	20.73	0.22	35.36	24.05	53.21	18.67	20.52	20.69	20.61	0.21	35.12	23.07	53.42
FeO	19.19	30.42	34.12	45.49	1.10	0.06	14.05	18.15	27.67	34.67	35.75	46.69	1.15	0.03	13.58
MnO	0.06	6.97	2.94	0.75	0.02	0.00	0.16	0.02	8.49	1.47	1.21	0.22	0.01	0.00	0.05
MgO	10.03	1.82	2.67	0.25	0.53	0.00	1.58	10.31	1.16	3.60	3.32	0.17	0.68	0.00	1.83
CaO	0.05	3.24	2.50	0.04	0.04	5.42	0.00	0.02	5.84	2.07	1.52	0.02	0.01	4.25	0.01
Na_2O	0.14	0.00	0.00	0.01	1.10	7.70	0.10	0.26	0.00	0.00	0.01	0.02	1.09	8.57	0.63
K_2O	8.90	0.00	0.00	0.05	9.55	0.02	0.01	8.99	0.01	0.00	0.00	0.12	9.61	0.04	0.00
Total	94.99	98.72	99.54	100.83	93.45	99.29	96.29	94.18	99.97	98.98	98.49	100.45	93.87	99.14	97.09
Si	2.72	2.95	2.97	0.00	3.05	2.76	7.54	2.73	2.96	2.97	2.96	0.00	3.06	2.81	7.54
Ti	0.10	0.00	0.00	1.01	0.03	0.00	0.11	0.12	0.00	0.00	0.00	1.00	0.04	0.00	0.15
Al	1.71	1.99	1.99	0.01	2.82	1.26	17.75	1.68	1.97	1.99	2.00	0.01	2.79	1.21	17.67
Fe^{2+}	1.22	2.10	2.32	0.94	0.06	0.00	3.33	1.16	1.89	2.36	2.46	0.98	0.06	0.00	3.19
Mn	0.00	0.49	0.20	0.02	0.00	0.00	0.04	0.00	0.59	0.10	0.08	0.00	0.00	0.00	0.01
Mg	1.13	0.22	0.32	0.01	0.05	0.00	0.67	1.17	0.14	0.44	0.41	0.01	0.07	0.00	0.76
Ca	0.00	0.29	0.22	0.00	0.00	0.26	0.00	0.00	0.51	0.18	0.13	0.00	0.00	0.20	0.00
Na	0.02	0.00	0.00	0.00	0.14	0.66	0.06	0.04	0.00	0.00	0.00	0.00	0.14	0.74	0.34
K	0.86	0.00	0.00	0.00	0.82	0.00	0.00	0.88	0.00	0.00	0.00	0.00	0.83	0.00	0.00
Sum	7.77	8.05	8.03	1.99	6.99	4.94	29.50	7.77	8.06	8.04	8.04	2.00	6.99	4.96	29.66
Oxygen	11	12	12	3	11	8	46	11	12	12	12	3	11	8	46
X_{Mg}	0.48	0.10	0.12	0.01	0.46	–	0.17	0.50	0.07	0.16	0.14	–	0.51	–	0.19
Ti (22O)	0.20	–	–	–	–	–	–	0.24	–	–	–	–	–	–	–
Sps	–	0.16	0.07	–	–	–	–	–	0.19	0.03	0.03	–	–	–	–
Prp	–	0.07	0.11	–	–	–	–	–	0.05	0.14	0.13	–	–	–	–
Grs	–	0.09	0.07	–	–	–	–	–	0.16	0.06	0.04	–	–	–	–
Alm	–	0.68	0.76	–	–	–	–	–	0.60	0.77	0.80	–	–	–	–

Table 3. Representative mineral compositions for samples W126 and W110. Syn-D_1 rim* for sample W110 refers to this analysis being representative of the assumed rim composition, which is the maximum pyrope value of Fig. 6d, as the low-Mg regions are interpreted as the result of post-peak diffusional modification. X_{Mg} = Mg/(Mg + Fe^{2+}), Ti (22O) is the Ti content per 22 oxygen, Sps = Mn/(Fe^{2+} + Mg + Ca + Mn), Prp = Mg/(Fe^{2+} + Mg + Ca + Mn), Grs = Ca/(Fe^{2+} + Mg + Ca + Mn), Alm = Fe^{2+}/(Fe^{2+} + Mg + Ca + Mn)

Sample	W126 (Ky-Sil)						W110 (Sil)					
Mineral	Bt	Grt	Grt	Ilm	Ms	Pl	Bt	Grt	Grt	Ilm	Ms	Pl
Location	matrix	syn-D_1 rim	post-D_1 rim	matrix	matrix	matrix	matrix	syn-D_1 rim*	post-D_1 rim	matrix	matrix	matrix
Analyses	8	1	1	2	5	4	5	1	1	2	4	5
SiO_2	35.25	36.90	36.43	0.09	46.30	63.23	35.28	36.19	35.55	0.13	44.92	62.07
TiO_2	2.27	0.00	0.01	53.24	0.80	0.02	3.00	0.00	0.01	54.32	0.85	0.01
Al_2O_3	18.48	20.90	21.00	0.19	35.93	22.91	18.93	20.60	20.16	0.18	34.76	23.75
FeO	18.80	34.15	35.53	46.70	1.04	0.03	19.70	32.33	34.33	45.78	1.16	0.04
MnO	0.01	2.61	2.04	0.39	0.00	0.00	0.11	4.67	3.98	0.90	0.01	0.00
MgO	9.90	3.79	2.89	0.29	0.54	0.00	8.93	3.46	2.60	0.18	0.60	0.00
CaO	0.01	1.33	2.21	0.02	0.00	4.02	0.00	1.89	1.67	0.03	0.01	5.07
Na_2O	0.24	0.00	0.00	0.03	0.91	8.82	0.23	0.00	0.00	0.10	0.80	7.93
K_2O	9.38	0.00	0.02	0.12	9.24	0.03	9.71	0.00	0.00	0.02	10.36	0.05
Total	94.34	99.68	100.13	101.07	94.76	99.06	95.90	99.13	98.30	101.66	93.46	98.93
Si	2.71	2.98	2.95	0.00	3.07	2.81	2.68	2.95	2.95	0.00	3.05	2.77
Ti	0.13	0.00	0.00	1.00	0.04	0.00	0.17	0.00	0.00	1.01	0.04	0.00
Al	1.67	1.99	2.01	0.01	2.81	1.20	1.70	1.98	1.97	0.01	2.79	1.25
Fe^{2+}	1.21	2.31	2.41	0.97	0.06	0.00	1.25	2.21	2.38	0.94	0.07	0.00
Mn	0.00	0.18	0.14	0.01	0.00	0.00	0.01	0.32	0.28	0.02	0.00	0.00
Mg	1.13	0.46	0.35	0.01	0.05	0.00	1.01	0.42	0.32	0.01	0.06	0.00
Ca	0.00	0.12	0.19	0.00	0.00	0.19	0.00	0.16	0.15	0.00	0.00	0.24
Na	0.04	0.00	0.00	0.00	0.12	0.76	0.03	0.00	0.00	0.00	0.11	0.69
K	0.92	0.00	0.00	0.00	0.78	0.00	0.94	0.00	0.00	0.00	0.90	0.00
Sum	7.80	8.03	8.05	2.00	6.93	4.97	7.79	8.05	8.06	1.99	7.01	4.95
Oxygens	11	12	12	3	11	8	11	12	12	3	11	8
X_{Mg}	0.48	0.17	0.13	–	0.48	–	0.45	0.16	0.12	–	0.48	–
Ti (22O)	0.26	–	–	–	–	–	0.34	–	–	–	–	–
Sps	–	0.06	0.05	–	–	–	–	0.10	0.09	–	–	–
Prp	–	0.15	0.11	–	–	–	–	0.14	0.10	–	–	–
Grs	–	0.04	0.06	–	–	–	–	0.05	0.05	–	–	–
Alm	–	0.75	0.78	–	–	–	–	0.71	0.76	–	–	–

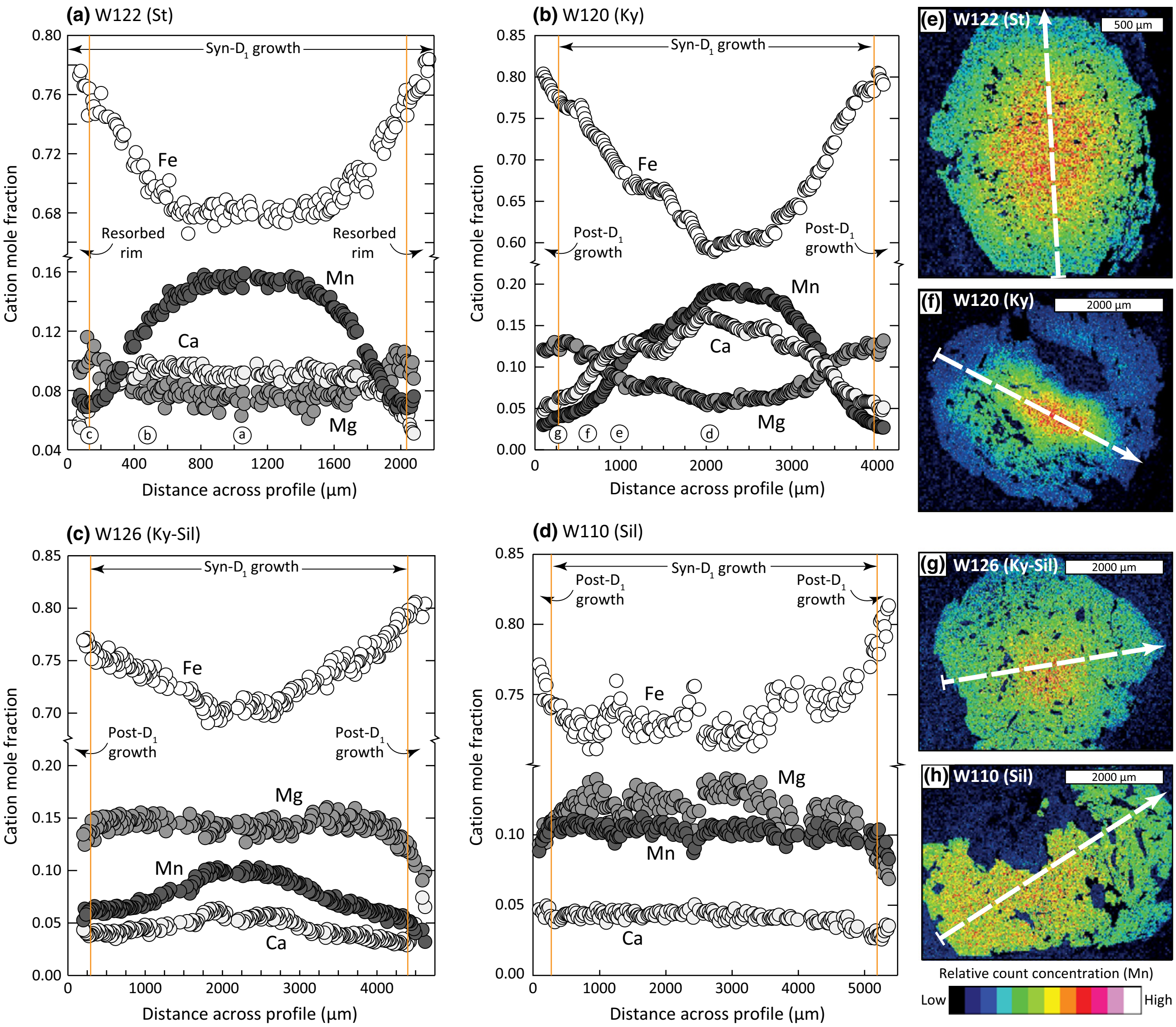

Fig. 6. Garnet porphyroblast compositional line profiles. (a–d) Rim-to-rim garnet composition profiles for samples W122, W120, W126 and W110, respectively. Line profiles are non-continuous due to traverses crossing inclusions and fractures; these analyses are absent from the profiles. The orange lines represent the peak-D_1 growth increment, inbound of minor resorption (W122) or post-D_1 garnet growth (W120, W126 & W110). Note that for sample W110, the maximum pyrope value is considered representative of peak-D_1; see text for details. The circled numbers on (a, b) correspond to the pyrope-grossular isopleth intersections used to reconstruct prograde growth history in Fig. 7b,d. (e–h) Corresponding garnet Mn X-ray maps, showing exact profile locations. The colour scale of relative counts is not comparable between images.

sequestration is a proxy for garnet growth (Kohn & Spear, 2000). The suggestion of two-stage garnet growth for the latter samples is consistent with the microstructural observations of post-D_1 garnet rims in kyanite- and higher grade samples (Fig. 4e).

The orange lines in Fig. 6a–d represent the inferred position of preserved peak-D_1 garnet composition. This is inbound of the resorbed rim for sample W122 (Fig. 6a), and marks the transition between syn- to post-D_1 garnet growth for samples W120, W126 and W110 in Fig. 6b–d, respectively. The orange lines are considered to best represent the peak-D_1 garnet chemistry, with the exception of sample W110, which is observed to have a relatively flat Ca profile in the syn-D_1 growth region, compared with spikes in Fe, Mg and Mn content (Fig. 6d), which occur where the analytical profile passes close to biotite-rich matrix embayments into the garnet grain (Fig. 6h). As Ca has been shown to undergo significantly slower intra-crystalline cation diffusion in garnet compared with Fe, Mg and Mn (Chernoff & Carlson, 1997), we interpret that these compositional spikes represent post-peak diffusional modification. Thus, we conclude that the garnet syn-D_1 growth composition in sample W110 was homogeneous at peak conditions, typical of sillimanite-grade pelitic lithologies (Woodsworth, 1977), with the maximum value of pyrope considered representative of the peak-D_1 composition, because Mg is expected to increase temperature (Spear, 1993).

THERMOBAROMETRY

Analytical techniques

Pseudosections were constructed for each of the study samples (W122, W120, W126 & W110), to provide a framework for understanding Barrovian mineral growth, and to constrain the *P–T* conditions of metamorphism. In addition, the Ti content of biotite geothermometer (Henry *et al*., 2005) was used as an independent check on peak conditions. This geothermometer was calibrated for graphitic metapelites that contain ilmenite or rutile as a Ti-saturating phase, so is ideally suited to this study. Compositional data used for these calculations (X_{Mg} and Ti content per 22 oxygen) are given in Tables 2 & 3.

Model system

All *P–T* and *T–X* pseudosections were constructed using THERMOCALC v3.33 and the internally consistent dataset tc-ds55 (Holland & Powell, 1998; updated to August, 2004). Modelling was performed in the 11-component system $MnO–Na_2O–CaO–K_2O–FeO–MgO–Al_2O_3–SiO_2– H_2O–TiO_2–Fe_2O_3$ (MnNCKFMASHTO) utilizing the following solid-solution models: silicate melt (White *et al*., 2007); cordierite, staurolite and chlorite (Mahar *et al*., 1997; Holland & Powell, 1998); garnet and biotite (Mn-bearing model, White *et al*. (2005)); chloritoid (Mahar *et al*., 1997; White, 2000); muscovite (Coggon & Holland, 2002); K-feldspar and plagioclase (Holland & Powell, 2003); epidote (Holland & Powell, 1998); and magnetite (subsolidus model; White, 2000). Additional phases with no solid solution include andalusite, kyanite, sillimanite, rutile, quartz and H_2O.

Calculating the bulk composition

Whole-rock XRF analyses (Table 1) were modified to calculate the bulk compositions for all pseudosections (Table 4), taking into consideration the effect of unmodelled accessory phases and oxides, fluid composition and ferric iron content. Relatively minor changes were required to convert the XRF analyses, as activity–composition models are available for all major phases in each sample in the MnNCKFMASHTO system (Fig. 5). First, P_2O_5 was removed from the bulk. This included a proportional adjustment to total CaO to correct for the contribution made by apatite ($CaPO_4$) to the CaO total, by assuming that half of the P_2O_5 resided in apatite (with the rest derived from monazite). Second, the fluid phase was set to be in excess, as only subsolidus regions were considered in the modelling. The activity of H_2O (a_{H_2O}) was set at 0.9, because all samples contain graphite, suggesting that the coexisting metamorphic fluid would have had a reduced a_{H_2O} as a result of dilution of the fluid phase with CO_2 (Ohmoto & Kerrick, 1977). Last, a value of $X_{Fe^{3+}} = 0.01$ was applied, because all of the samples only contain ilmenite as an oxide, which Diener & Powell (2010) showed indicates highly reducing conditions. A fractionating bulk composition was not considered, because garnet mode is low in all samples (<3%).

Results

Figures 7 & 8 show the combined results of the thermobarometric analysis for each of the study samples, with *P–T* pseudosections overlain by the results of the Henry *et al*. (2005) geothermometer. The general topology of all of the pseudosections is similar, with the low-variance fields bounding the staurolite stability field providing a focal point to each diagram. These fields correspond to the reactions governing the growth and breakdown of staurolite, and are essentially equivalent to the discontinuous AFM reactions (Powell *et al*., 1998):

$$\mathrm{Grt + Chl + Ms = St + Bt + Qz + H_2O} \quad (1)$$

$$\mathrm{St + Bt + Qz = Als + Ms + Grt + H_2O} \quad (2)$$

Isopleths of garnet modal proportion are shown on each pseudosection and quantify the degree of consumption or growth that occurs across each of these reactions. For each sample, a calculated assemblage field was determined that matched the observed peak assemblage (red assemblage labels, Figs 7 & 8). The calculated peak assemblages show an excellent fit with the Henry *et al*. (2005) geothermometer results,

Table 4. Compositions used as the input to THERMOCALC in the system MnNCKFMASHTO for all pseudosections (mol.%). H_2O was considered to be present in excess in all pseudosections. Note that THERMOCALC treats $Fe_2O_3 = 2 \cdot FeO + O$. Therefore, $X_{Fe^{3+}} = 2 \cdot O/FeO$.

Figure	Sample	SiO_2	Al_2O_3	CaO	MgO	FeO	K_2O	Na_2O	TiO_2	MnO	O	a_{H_2O}	$X_{Fe^{3+}}$
7a,b	W122 (St)	63.83	15.86	0.68	6.08	8.19	3.17	1.18	0.88	0.09	0.04	0.9	0.01
7c,d	W120 (Ky)	70.33	12.41	0.42	5.34	6.59	3.28	0.90	0.60	0.10	0.03	0.9	0.01
8a,b	W126 (Ky-Sil)	71.36	11.88	1.07	4.70	5.57	2.68	2.07	0.57	0.07	0.03	0.9	0.01
8c,d	W110 (Sil)	67.51	13.61	0.29	6.07	7.05	3.77	0.70	0.88	0.07	0.04	0.9	0.01
9a	W110 (Sil)	67.51	13.61	0.29	6.07	7.05	3.77	0.70	0.88	0.07	0.04	1.0	0.01
9b	W110 (Sil)	67.54	13.62	0.29	6.08	7.05	3.78	0.70	0.88	0.07	0.00	0.9	0.00
9b	W110 (Sil)	67.30	13.57	0.29	6.06	7.03	3.76	0.69	0.88	0.07	0.35	0.9	0.10

as the calculated temperature for each sample intersects the calculated peak assemblage field (green lines, Figs 7 & 8). The peak assemblage fields are further constrained by consideration of the syn-D_1 garnet rim chemistry for each of the samples (Fig. 6), with the red polygons delimiting the regions that satisfy grossular and pyrope isopleth constraints (±0.01 of the syn-D_1 garnet rim values in Tables 2 & 3) and the Henry *et al.* (2005) geothermometer results (which has calculated errors of ±24 °C below 600 °C, and ±23 °C between 600–700 °C). These red polygons are considered to approximate the peak conditions for each of the samples. For sample W122 (Fig. 7a,b), a more conservative polygon is applied, due to considerations of garnet resorption (detailed below). Finally, segments of the prograde *P–T* path are calculated for samples W122 and W120, by matching the garnet compositional zoning in Fig. 6a, b (circled letters at the base of the profiles) to the calculated pyrope and grossular garnet isopleths in Fig. 7b,d, respectively.

W122 (St)

It is notable in Fig. 7a that the biotite-in reaction occurs at a higher temperature for sample W122, compared with that for kyanite-bearing sample W120 on Fig. 7c. Sample W122 has the most aluminous bulk composition, which Tinkham *et al.* (2001) showed reduces biotite stability relative to chlorite. Given that biotite is petrographically observed to predate garnet growth, this suggests an upper pressure limit of ~4.3 kbar on the incoming of garnet for this sample (Fig. 7a). Garnet core isopleths meet this requirement (Table 2), with grossular, pyrope and garnet-in intersecting within several hundred bars in a biotite-bearing field at ~3.5 kbar and 530 °C (point a, Fig. 7b). The proposed *P–T* path segment from this point is steep and clockwise, culminating just within the peak assemblage field at ~4.8 kbar and 560 °C (point c, Fig. 7b). However, garnet rim chemistry is unlikely to represent peak conditions, because garnet mode decreases between the staurolite-in and chlorite-out boundaries (as required by Eq. 1), which is the likely cause of the resorbed rim observed in Fig. 6a. Even if the effects of resorption were corrected for, only certain trajectories following consumption of chlorite would result in renewed garnet growth. Therefore, the Henry *et al.* (2005) geothermometer is considered a more reliable estimate of peak temperature. Alongside pressure constraints imposed by garnet mode in the peak assemblage field, peak conditions of ~5.2 kbar and 580 °C are suggested for sample W122.

W120 (Ky)

Figure 7c suggests a narrow temperature field within which sample W120 could have developed its peak assemblage, which is in good agreement with the geothermometer calculation of Henry *et al.* (2005) (Fig. 7d). As for sample W122, garnet core isopleths (Table 2) intersect within several hundred bars of the predicted garnet-in boundary, which imposes a constraint on the start of garnet growth at 4.5 kbar and 520 °C (point d, Fig. 7d). Several waypoints are identified on Fig. 6b, which suggest a relatively linear partial *P–T* path that culminates within 10 °C of the low-pressure end of the calculated peak assemblage field (point g, Fig. 7d). Waters & Lovegrove (2002) and Powell & Holland (2008) discussed the sources of error in the calculation of pseudosections, and concluded that a realistic assessment of uncertainty on all *P–T* estimates is probably at least ±0.5 kbar and ±25 °C, so this point is considered within error of the peak assemblage field. The proposed *P–T* path crosses a region of predicted minor garnet resorption at pyrope = 0.10 (Fig. 7d), which was not observed on Fig. 6b. Otherwise, garnet is predicted to grow throughout the staurolite window, as it has a trajectory slightly steeper than garnet mode.

W126 (Ky-Sil) and W110 (Sil)

Given that garnet in the higher grade samples is variably homogenized, only peak estimates of ~6.3 kbar at 650 °C (Fig. 8b) and ~6.0 kbar at 670 °C (Fig. 8d) are calculated for samples W126 and W110, respectively.

Changing model parameters for sample W110

The effects of variable a_{H_2O} and $X_{Fe^{3+}}$ are explored for sample W110 to assess the dependency of the results on the bulk composition and to explore the implications for Barrovian sequences (Fig. 9). Figure 9a was calculated with the same bulk composition as Fig. 8c, but with an a_{H_2O} of unity. Comparison between the two figures shows that the general effect of reduced a_{H_2O} is to lower the temperature of most of the mineral assemblage boundaries and increase the solidus temperature. The net effect is to widen the sub-solidus aluminosilicate stability window from ~20 °C width at $a_{H_2O} = 1.0$ to ~60 °C at $a_{H_2O} = 0.9$. This implies that variable a_{H_2O} could have an important effect on the spacing of isograds, and influence which aluminosilicate is present at the onset of anatexis.

The effect of $X_{Fe^{3+}}$ is quantified in a T–$X_{Fe^{3+}}$ pseudosection for sample W110 at 6 kbar that spans $X_{Fe^{3+}} = 0.0$–0.1 (Fig. 9b). Magnetite is calculated to join all assemblages at $X_{Fe^{3+}} = 0.05$–0.09, which indicates that oxides are a good indicator of redox state (Diener & Powell, 2010). While most pelitic metamorphic minerals are relatively unaffected by oxidation state (White, 2000; Diener & Powell, 2010), Fig. 9b shows that more oxidized bulk compositions reduce the stability of garnet, with garnet-out

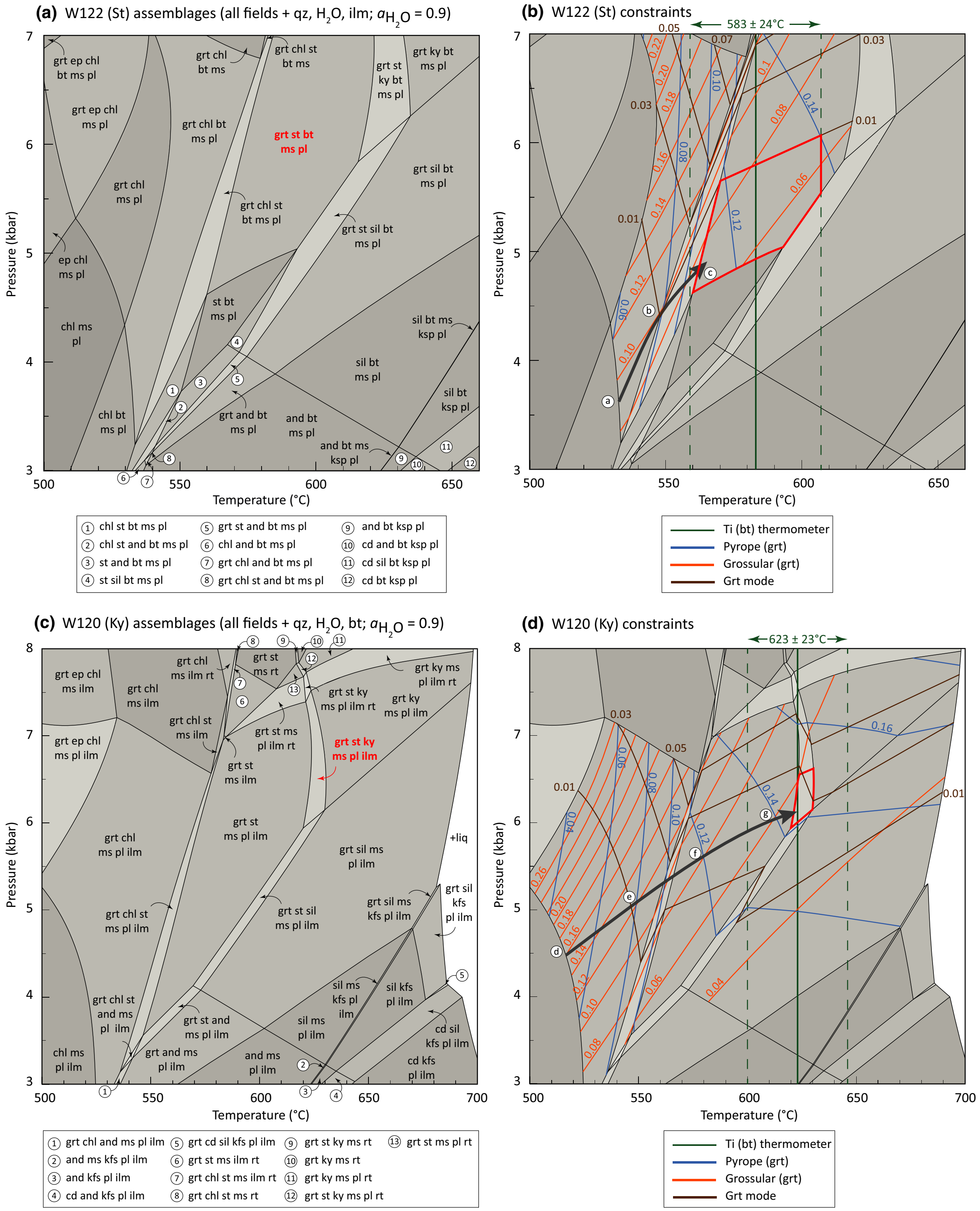

Fig. 7. Pseudosection analysis for samples W122 and W120. Supra-solidus regions are not shown for clarity. All diagrams have the same aspect ratio, so gradients are comparable. (a) Sample W122 pseudosection, with all assemblage fields labelled. The observed peak assemblage is shown in red. (b) Corresponding diagram showing constraints for sample W122. Relevant fields are contoured for pyrope and grossular isopleths and garnet mode, and the diagram is overlain by the Henry *et al.* (2005) Ti-in-biotite thermometer calculation (legend, bottom right). Garnet compositions from Fig. 6a and Table 2 are used to draw a partial prograde *P–T* path, and to delimit the peak assemblage field. The red polygon represents the region where all constraints are met, and is considered to represent the peak conditions for this sample. (c) Sample W120 pseudosection, with all assemblage fields labelled. The observed peak assemblage is shown in red. (d) Logic as Fig. 7b, but for sample W120 and using garnet compositional constraints from Fig. 6b.

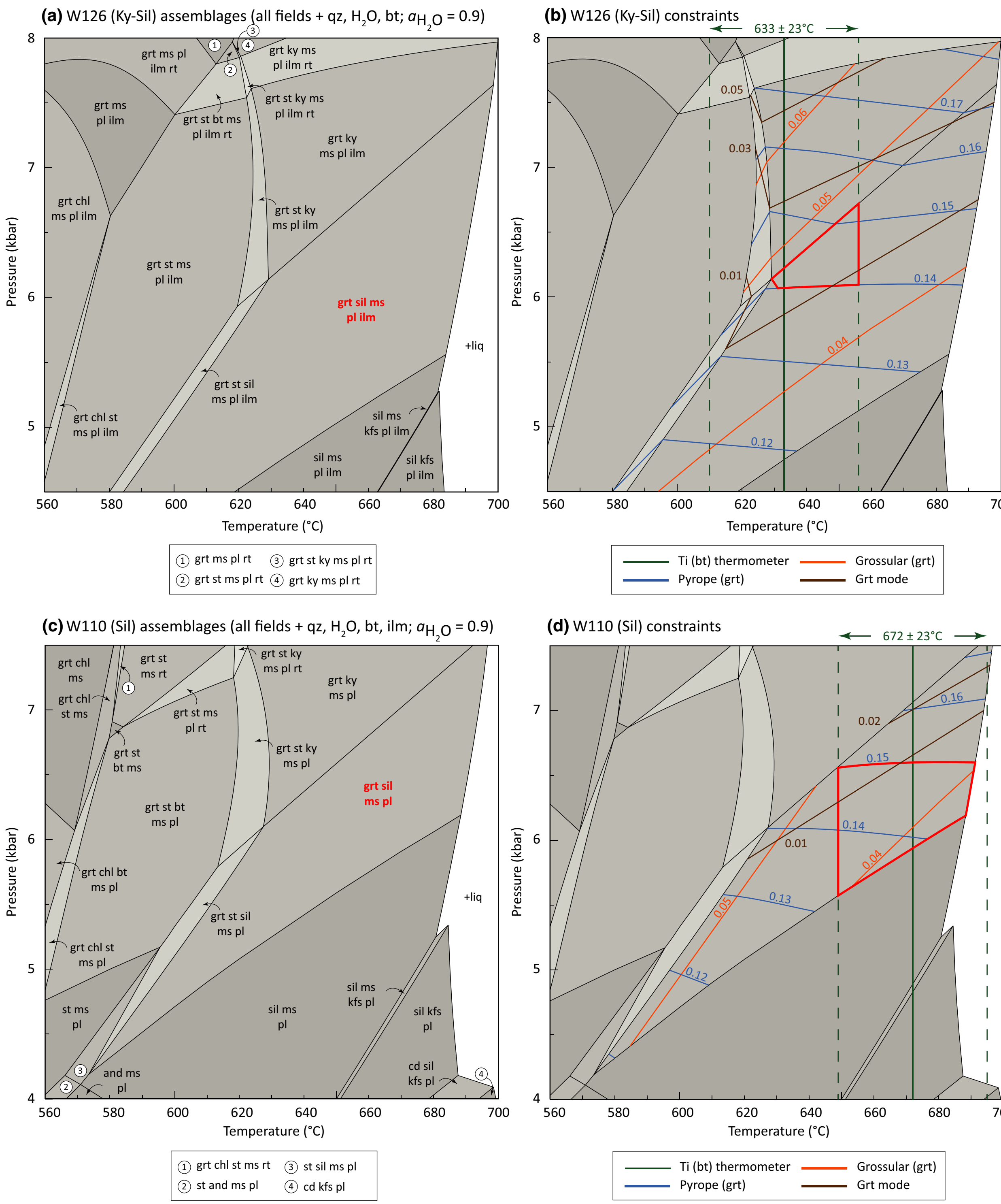

Fig. 8. Pseudosection analysis for samples W126 and W110. Supra-solidus regions are not shown for clarity. All diagrams have the same aspect ratio, so gradients are comparable. (a) Sample W126 pseudosection, with all assemblage fields labelled. The observed peak assemblage is shown in red. (b) Corresponding diagram showing constraints for sample W126. Relevant fields are contoured for pyrope and grossular isopleths and garnet mode, and the diagram is overlain by the Henry *et al.* (2005) Ti-in-biotite thermometer calculation (legend, bottom right). Garnet compositions from Table 3 are used to delimit the peak assemblage field. The red polygon represents the region where all constraints are met, and is considered to represent the peak conditions for this sample. (c) Sample W110 pseudosection, with all assemblage fields labelled. The observed peak assemblage is shown in bold. (d) Logic as Fig. 8b, but for sample W110. Note that for sample W110, the maximum pyrope value of Fig. 6d is considered representative of the peak-D_1 value in Table 3, as the low-Mg regions are interpreted as the result of post-peak diffusional modification.

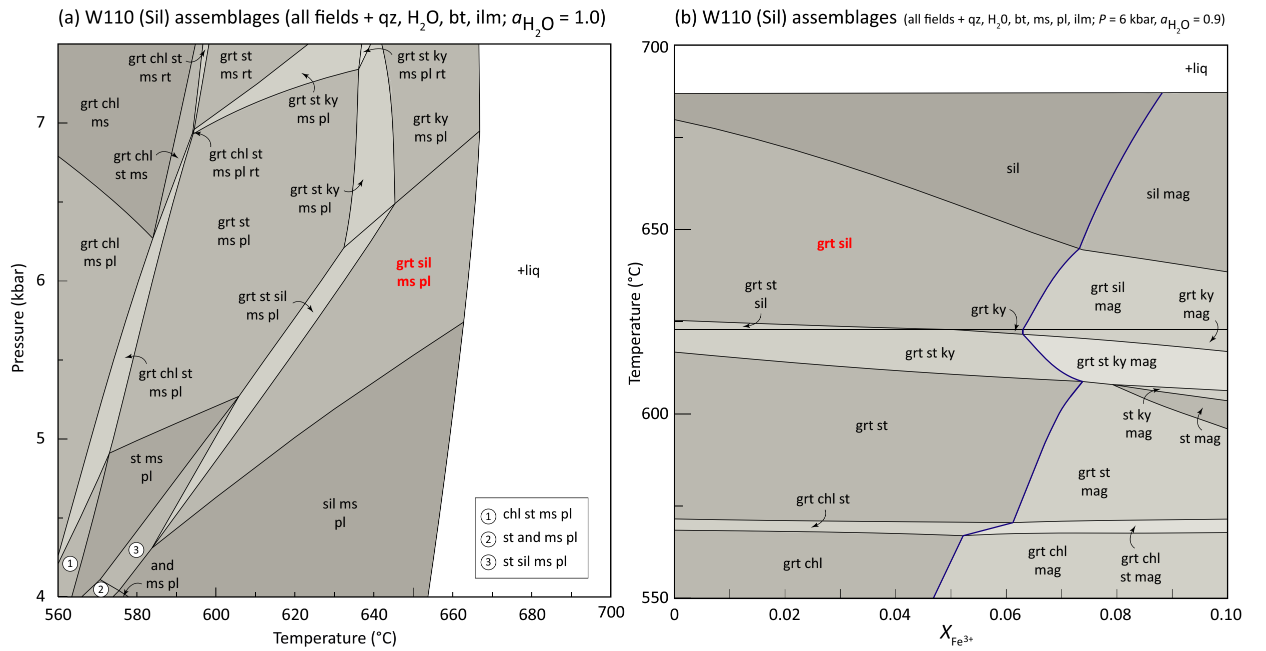

Fig. 9. Changing model parameters for sample W110. (a) Sample W110 pseudosection, with all assemblage fields labelled. The observed W110 assemblage is shown in red. The bulk composition is the same as the pseudosection in Fig. 7c, except that a_{H_2O} has increased from 0.9 to unity. (b) T–$X_{Fe^{3+}}$ diagram for sample W110 at 6 kbar, with $X_{Fe^{3+}}$ = 0–0.1. The observed W110 assemblage is shown in red. As $X_{Fe^{3+}}$ increases, garnet is observed to be less stable, and magnetite (blue line) is calculated to join all assemblages.

decreasing from ~680 °C to ~640 °C as $X_{Fe^{3+}}$ increases from 0 to 0.1. This is likely due to the increased amount of Fe locked up in oxides and the consequent increase of X_{Mg} in the normal ferromagnesian minerals (Chinner, 1960).

U–Th–Pb MONAZITE GEOCHRONOLOGY

U–Th–Pb dating of monazite was conducted for each of the study samples (W122, W120, W126 & W110), to investigate the relative timing of metamorphic mineral growth between samples, to resolve the timing of the sillimanite-grade metamorphism and ultimately to reveal the timescales of Barrovian metamorphism in the DSC. In general, monazite occurs in pelitic bulk compositions both at low and high grades, with allanite more stable at intermediate *P–T* conditions (Janots *et al.*, 2008). For example, allanite has been observed to form at the expense of low-grade monazite roughly coincidental with the biotite isograd (Wing *et al.*, 2003), and several studies have documented the growth of high-grade monazite at staurolite-grade *P–T* conditions (e.g. Smith & Barreiro, 1990; Kohn & Malloy, 2004; Berman *et al.*, 2005). However, the allanite-monazite transitions are thought to be strongly dependent on bulk composition, with CaO and Al_2O_3 in particular cited as important variables (Wing *et al.*, 2003; Janots *et al.*, 2007; Spear, 2010). This study has the advantage that chemically similar metapelites were sampled from different metamorphic grades, which is reflected by a consistent pattern of allanite–monazite relations with grade in the DSC, with allanite observed to be stable from biotite grade, but replaced by monazite from staurolite grade onwards (Table 1).

Analytical techniques

In situ U–Th–Pb analysis of monazite was carried out on the Sensitive High Resolution Ion Microprobe (SHRIMP) at the Geological Survey of Canada (GSC). Automated full thin section scans with a 5 μm step size were performed on the GSC's Zeiss Evo SEM to locate monazite suitable for geochronological analysis. Targets from petrographically significant areas were then prepared for analysis according to the methods of Rayner & Stern (2002). Three petrographic positions were analysed: syn-D_1 garnet, matrix and post-D_1 garnet (using the terminology developed above). Examples of each of these positions are shown in Fig. 10a–j. Enhanced contrast back scattered electron (BSE) images were generated for each monazite grain to identify internal compositional domains, where present, and to guide analytical spot localities. Monazite analysis employed the method described in Stern & Berman (2000). Analytical details regarding spot size, data reduction protocol and U–Th–Pb calibration are reported in Table 5. Isoplot (Ex version 3.00; Ludwig, 2003) was used to

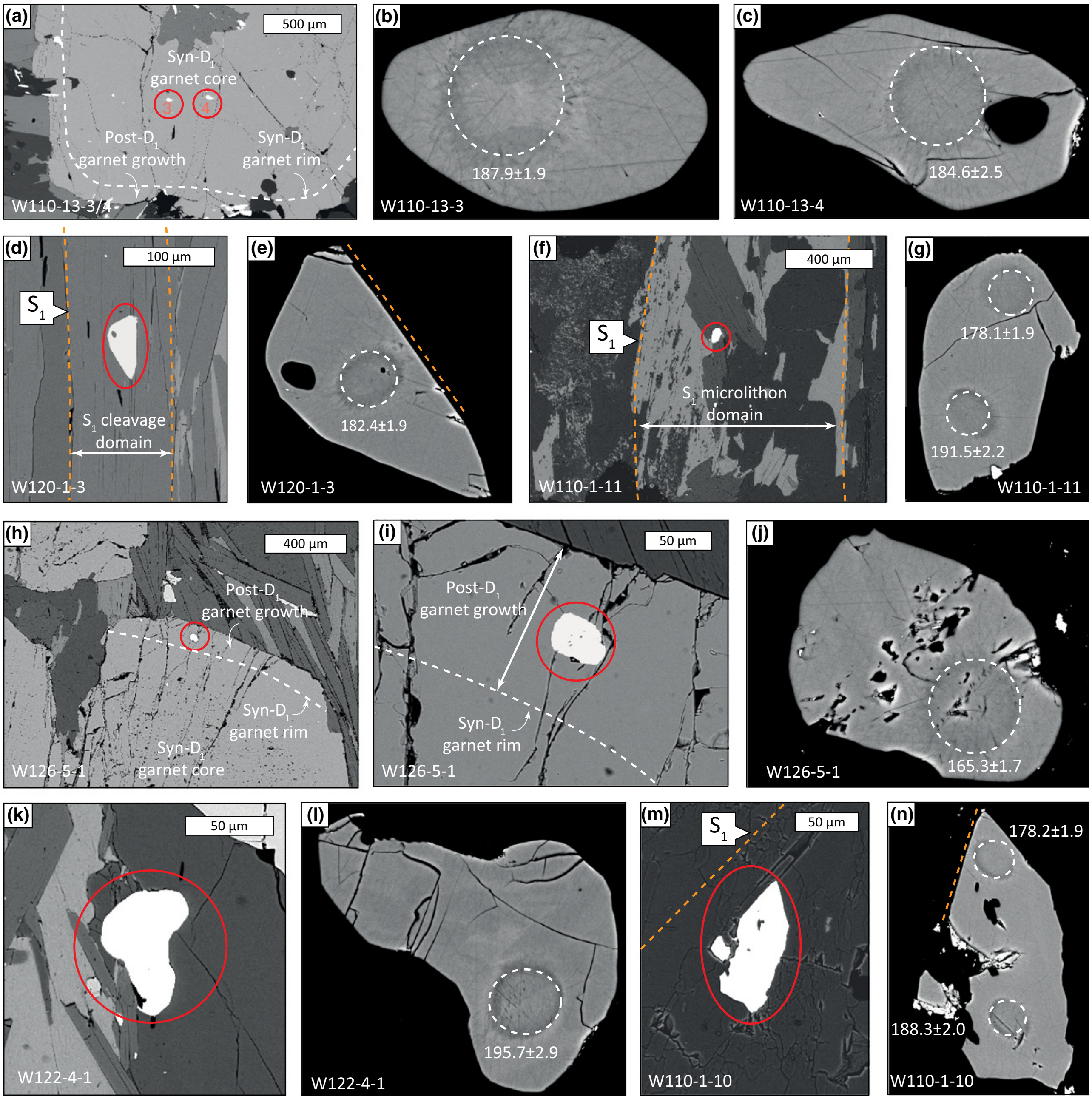

Fig. 10. Back-scattered electron (BSE) images of monazite. Spot sizes have a diameter of 16 μm (dotted white circles). The monazite grains are labelled following the convention w-x-y; where w = sample number, x = slide number, y = grain number. (a) Example of monazite inclusions in syn-D_1 garnet, with a close-up of the grains shown in (b, c). (d) Example of a monazite grain in the S_1 cleavage domain of the matrix, with a close-up of the grain in (e). The grain is aligned within the S_1 fabric (dotted orange line). (f) Example of a monazite grain in the S_1 microlithon domain of the matrix, with a close-up of the grain in (g). (h) Example of a monazite inclusion in post-D_1 garnet, with close-ups in (i) and (j). The post-D_1 garnet rims overgrow the S_1 fabric and have a distinct chemistry; see text for details. (k, l) Example of a monazite grain that is homogeneous in BSE, but displays significant variation in age. The younger spot is in the part of the grain that is strongly faceted adjacent a sillimanite needle, which aligns with S_1. (m, n) Example of a monazite grain from W122, with a characteristic slightly mottled appearance in BSE.

generate all Tera-Wasserburg diagrams and regressed ages with related statistics. Major and trace element compositions of analysed monazite grains are presented in Table S1 following the methods given above for mineral analyses.

Results

Results are presented as Tera-Wasserburg plots and as probability density diagrams plus histograms (Fig. 11), with the underlying data shown in Table 5. The

Table 5. U–Th–Pb monazite geochronology data for samples W122, W120, W126 and W110. Notes: analysis name follows the convention w-x-y.z; where w = sample number, x = slide number, y = grain number and z = spot number. Uncertainties reported at 1σ, calculated using SQUID 2.22.08.04.30. f(206)^{207} refers to the mole percent of total ^{206}Pb that is due to common Pb, calculated using the ^{207}Pb-method; Stacey & Kramers (1975) model common Pb composition (t = 220 Ma) was used. * refers to radiogenic Pb (corrected for common Pb). Calibration standard 8153; U = 2065 ppm; U–Pb age = 512 Ma; Th–Pb age = 507 Ma. Error in ^{208}Pb/^{232}Th calibration 1.35% (included); error in ^{206}Pb/^{238}U calibration 1.02% (included). Analytical details: mounts IP643 and IP644, 16 μm diameter spot, 1.0 nA O^{2-} primary beam, six scans. Standard error in calibration was 0.6% for Th–Pb and 0.5% for U–Pb (not included in above errors but required when comparing data from different mounts).

													Ratios								Ages (Ma)			
													Uncorrected						^{204}Pb corr.		^{204}Pb corr.		^{207}Pb corr.	
Analysis	Petrographic position	U (ppm)	Th (ppm)	$\frac{^{232}Th}{^{238}U}$	^{206}Pb* (ppm)	$\frac{^{204}Pb}{^{206}Pb}$	1σ(%)	$\frac{^{208}Pb}{^{206}Pb}$	1σ (%)	f(206)^{207}(%)	$\frac{^{208}Pb^*}{^{206}Pb^*}$	1σ(%)	$\frac{^{238}U}{^{206}Pb}$	1σ(%)	$\frac{^{207}Pb}{^{206}Pb}$	1σ(%)	$\frac{^{208}Pb}{^{232}Th}$	1σ(%)	$\frac{^{208}Pb}{^{232}Th^*}$	1σ(%)	$\frac{^{208}Pb}{^{232}Th}$	1σ(abs)	$\frac{^{206}Pb}{^{238}U}$	1σ(abs)
W122-1-4.2	matrix	4195	40903	10.1	104	3.2E-3	5.1	3.19	0.44	5.9	3.26	0.44	32.542	1.4	0.09294	2.10	0.0097	1.6	0.00936	1.6	188.3	2.9	184.7	2.7
W122-1-5.2	matrix	3523	46340	13.6	89	5.9E-4	15.8	4.36	0.43	1.1	4.39	0.43	33.791	1.4	0.05567	1.26	0.0095	1.6	0.00945	1.6	190.1	3.0	186.6	2.7
W122-5-3.1	matrix	3264	35726	11.3	84	2.5E-4	58.4	3.55	0.45	0.5	3.55	0.45	33.284	1.4	0.05402	1.25	0.0094	1.6	0.00939	1.6	188.9	3.0	189.9	2.7
W122-1-4.1	matrix	4213	39212	9.6	108	1.1E-3	8.4	3.09	0.41	2.0	3.11	0.41	32.699	1.5	0.06211	1.03	0.0098	1.9	0.00968	1.9	194.8	3.7	191.3	2.9
W122-1-5.1	matrix	3688	44546	12.5	96	1.0E-3	10.1	3.85	0.41	1.9	3.89	0.41	32.228	1.4	0.06232	1.10	0.0096	1.6	0.00949	1.6	190.9	3.0	194.0	2.8
W122-4-1.1	matrix	4093	38922	9.8	108	6.0E-4	12.5	3.15	0.41	1.1	3.16	0.41	32.169	1.5	0.05664	1.07	0.0100	1.6	0.00989	1.6	199.0	3.1	195.7	2.9
W120-2-24.1	post-D$_1$ garnet	5054	35452	7.2	107	5.5E-4	13.8	2.35	0.46	1.0	2.35	0.46	39.998	1.0	0.05369	1.13	0.0081	1.1	0.00802	1.1	161.6	1.7	158.3	1.6
W120-1-1.1	post-D$_1$ garnet	4805	32789	7.1	108	7.8E-4	12.0	2.34	0.50	1.4	2.34	0.50	37.709	1.0	0.05929	1.17	0.0088	1.1	0.00867	1.1	174.5	1.9	166.7	1.7
W120-5-2.1	post-D$_1$ garnet	4819	38768	8.3	114	7.9E-4	13.4	2.64	0.51	1.5	2.65	0.51	35.636	1.1	0.05725	2.11	0.0089	1.1	0.00881	1.1	177.3	1.9	176.7	1.9
W120-1-2.3	matrix	3631	32609	9.3	89	9.7E-4	11.9	2.99	0.49	1.8	3.00	0.49	34.605	1.0	0.05891	1.24	0.0093	1.1	0.00918	1.1	184.7	2.0	181.6	1.9
W120-1-3.1	matrix	2863	31306	11.3	70	6.3E-4	17.5	3.57	0.49	1.2	3.59	0.49	34.613	1.0	0.05501	1.35	0.0091	1.1	0.00907	1.1	182.6	2.0	182.4	1.9
W120-1-6.1	matrix	3309	34197	10.7	81	5.4E-4	16.0	3.41	0.45	1.0	3.42	0.45	34.533	1.0	0.05208	1.25	0.0092	1.2	0.00919	1.2	184.8	2.2	183.5	1.9
W120-1-2.2	matrix	3699	35854	10.0	92	5.2E-4	16.5	3.18	0.47	1.0	3.19	0.47	34.100	1.1	0.05554	1.26	0.0093	1.1	0.00926	1.1	186.4	2.0	185.0	2.1
W120-1-2.1	matrix	3349	28626	8.8	84	4.0E-4	23.6	2.74	0.50	0.7	2.74	0.50	33.951	1.0	0.05323	1.29	0.0091	1.1	0.00908	1.1	182.7	2.0	186.3	1.9
W120-1-6.2	matrix	3548	39832	11.6	89	4.6E-4	20.1	3.66	0.46	0.9	3.67	0.46	33.832	1.0	0.05489	1.27	0.0093	1.2	0.00927	1.2	186.5	2.3	186.6	1.9
W120-5-1.1	syn-D$_1$ garnet	3879	38808	10.3	97	6.0E-4	13.7	3.31	0.43	1.1	3.32	0.43	33.814	1.0	0.05209	1.20	0.0095	1.3	0.00941	1.3	189.2	2.5	187.4	1.9
W126-5-1.1	post-D$_1$ garnet	4886	30281	6.4	109	4.6E-4	14.2	2.05	0.47	0.9	2.05	0.47	38.245	1.0	0.05474	1.08	0.0084	1.1	0.00832	1.1	167.4	1.8	165.3	1.7
W126-2-7.1	matrix	6762	26316	4.0	155	4.3E-4	15.5	1.28	0.92	0.8	1.27	0.92	37.286	1.0	0.05629	1.07	0.0085	1.2	0.00840	1.2	169.0	2.0	169.2	1.7
W126-2-4.1	matrix	7880	27181	3.6	183	3.7E-4	17.1	1.14	0.55	0.7	1.13	0.55	36.711	1.0	0.05457	1.01	0.0087	1.1	0.00857	1.1	172.5	1.8	172.2	1.8
W126-3-3.1	matrix	6894	35154	5.3	166	3.6E-4	12.8	1.66	0.41	0.7	1.66	0.41	35.341	1.0	0.05262	0.89	0.0089	1.1	0.00884	1.1	177.8	1.9	179.2	1.8
W126-2-4.2	matrix	6856	25912	3.9	167	2.0E-4	19.7	1.27	0.49	0.4	1.26	0.49	35.058	1.0	0.05303	0.95	0.0092	1.0	0.00919	1.1	184.8	1.9	180.6	1.8
W126-3-2.1	syn-D$_1$ garnet	8138	46124	5.9	202	4.6E-4	11.1	1.75	0.41	0.9	1.74	0.41	34.343	1.0	0.05297	0.91	0.0087	1.0	0.00860	1.1	173.1	1.8	184.3	1.9
W126-2-8.1	matrix	5043	28917	5.9	126	3.3E-4	22.3	1.92	0.53	0.6	1.92	0.53	34.204	1.0	0.05341	1.20	0.0095	1.1	0.00942	1.1	189.5	2.0	184.9	1.9
W126-2-5.1	matrix	3987	24128	6.3	100	6.4E-4	21.5	1.92	0.57	1.2	1.92	0.57	33.931	1.0	0.05647	2.86	0.0091	1.1	0.00895	1.1	180.2	2.0	185.7	2.0
W126-2-7.2	matrix	4609	26722	6.0	117	4.9E-4	15.6	1.85	0.51	0.9	1.84	0.51	33.495	1.0	0.05888	1.10	0.0092	1.1	0.00911	1.1	183.3	2.0	187.5	1.9
W126-5-3.1	matrix	3897	41984	11.1	98	1.6E-3	8.6	3.51	0.49	2.9	3.56	0.49	33.008	1.2	0.06838	1.20	0.0096	1.1	0.00940	1.1	189.1	2.1	188.0	2.2
W126-5-2.1	syn-D$_1$ garnet	4999	47398	9.8	128	7.0E-4	10.7	3.27	0.39	1.3	3.28	0.39	33.060	1.0	0.05906	2.52	0.0101	1.1	0.01001	1.1	201.3	2.1	189.9	2.0
W126-2-6.1	matrix	4606	27863	6.3	119	3.5E-4	20.2	1.96	0.52	0.6	1.96	0.52	33.088	1.0	0.05328	1.21	0.0095	1.1	0.00943	1.1	189.7	2.1	191.1	2.0
W126-1-1.1	syn-D$_1$ garnet	4771	56532	12.2	124	4.9E-4	14.9	4.02	0.38	0.9	4.04	0.38	32.689	1.0	0.05353	1.09	0.0101	1.1	0.01001	1.1	201.3	2.1	193.4	2.0
W110-13-1.1	matrix	4236	34919	8.5	99	3.3E-4	20.2	2.68	0.51	0.6	2.69	0.51	36.696	1.0	0.05296	1.31	0.0086	1.1	0.00855	1.1	172.0	1.9	172.6	1.8
W110-1-11.2	matrix	3290	43037	13.5	79	6.9E-4	13.0	4.08	0.50	1.3	4.11	0.50	35.503	1.1	0.05393	1.45	0.0085	1.1	0.00845	1.1	170.1	1.9	178.1	1.9
W110-1-10.2	matrix	3328	36785	11.4	80	5.8E-4	20.1	3.59	0.51	1.1	3.61	0.51	35.422	1.0	0.05549	1.39	0.0089	1.1	0.00883	1.1	177.7	1.9	178.2	1.9
W110-8-6.2	matrix	4257	35103	8.5	103	4.0E-4	19.2	2.74	0.47	0.7	2.75	0.47	35.351	1.0	0.05158	1.24	0.0091	1.1	0.00905	1.1	182.1	1.9	179.4	1.9
W110-8-2.1	matrix	2559	34729	14.0	62	8.0E-4	15.0	4.50	0.54	1.5	4.54	0.54	35.052	1.1	0.05529	1.60	0.0092	1.1	0.00910	1.1	183.0	2.0	180.1	1.9
W110-1-9.1	matrix	5895	36492	6.4	144	4.7E-4	14.6	2.01	0.47	0.9	2.01	0.47	34.808	1.0	0.05562	1.06	0.0090	1.1	0.00895	1.1	180.2	2.0	181.3	1.9
W110-1-6.1	syn-D$_1$ garnet	3223	38929	12.5	80	5.3E-4	16.6	3.94	0.48	1.0	3.95	0.48	34.433	1.0	0.05568	1.34	0.0092	1.3	0.00911	1.3	183.4	2.3	183.2	1.9
W110-8-5.1	syn-D$_1$ garnet	3047	32292	11.0	76	4.0E-3	5.0	3.51	0.47	7.4	3.62	0.47	32.007	1.0	0.10934	1.58	0.0100	1.2	0.00958	1.2	192.6	2.4	183.7	2.0
W110-13-4.1	syn-D$_1$ garnet	2742	36758	13.9	68	6.6E-4	22.6	4.31	0.73	1.2	4.34	0.73	34.253	1.4	0.05369	1.47	0.0091	1.3	0.00903	1.3	181.6	2.3	184.6	2.5
W110-13-1.2	matrix	2596	36600	14.6	65	6.3E-4	17.9	4.49	0.55	1.2	4.52	0.55	33.962	1.1	0.05360	1.63	0.0091	1.1	0.00904	1.1	181.8	2.0	186.2	2.0
W110-1-5.1	syn-D$_1$ garnet	6913	26667	4.0	175	2.5E-4	18.7	1.24	0.70	0.5	1.23	0.70	33.855	1.0	0.05280	1.35	0.0092	1.0	0.00910	1.1	183.1	1.9	187.0	1.9
W110-8-6.1	matrix	3131	36854	12.2	79	8.9E-4	13.1	3.73	0.51	1.6	3.76	0.51	33.601	1.1	0.05829	1.40	0.0091	1.1	0.00904	1.1	181.9	2.0	187.1	2.0
W110-11-2.1	syn-D$_1$ garnet	3295	34822	10.9	83	4.5E-4	17.8	3.32	0.50	0.8	3.33	0.50	33.694	1.1	0.05438	1.35	0.0090	1.1	0.00897	1.1	180.6	2.0	187.5	2.0
W110-13-2.1	matrix	3230	34682	11.1	82	4.9E-4	22.2	3.51	0.51	0.9	3.53	0.51	33.629	1.1	0.05585	1.41	0.0094	1.1	0.00937	1.1	188.5	2.1	187.5	2.0
W110-13-3.1	syn-D$_1$ garnet	3863	35608	9.5	98	5.9E-4	13.9	3.03	0.46	1.1	3.04	0.46	33.554	1.0	0.05580	1.19	0.0095	1.1	0.00940	1.1	189.1	2.0	187.9	1.9
W110-8-4.1	matrix	4852	36137	7.7	123	5.3E-4	12.1	2.48	0.41	1.0	2.48	0.41	33.589	1.0	0.05481	1.02	0.0096	1.1	0.00950	1.1	191.1	2.0	188.0	1.9
W110-1-10.1	matrix	2252	32822	15.1	57	3.8E-4	30.2	4.80	0.53	0.7	4.82	0.53	33.599	1.1	0.05328	1.62	0.0095	1.1	0.00946	1.1	190.3	2.1	188.3	2.0
W110-1-11.1	matrix	5850	36045	6.4	151	4.9E-4	14.5	1.93	0.82	0.9	1.93	0.82	32.944	1.2	0.05521	1.04	0.0092	1.1	0.00909	1.1	183.0	1.9	191.5	2.2

$^{206}Pb/^{238}U$ ages are not observed to be systematically older than $^{208}Pb/^{232}Th$ ages, suggesting that excess ^{206}Pb is not significant (Schärer, 1984). $^{206}Pb/^{238}U$ ages are used for subsequent analysis because of smaller associated analytical errors than $^{208}Pb/^{232}Th$ ages (Table 5).

W122 (St)

Monazite grains in staurolite-grade sample W122 are located only in the matrix and are typically anhedral, with a slightly mottled appearance in BSE (Fig. 10k, l). A regression through five analyses of four separate grains from sample W122 yields a lower intercept age of 191.5 ± 2.4 Ma (Fig. 11a). Analysis W122-1-4.2 was excluded from the regression as it contains high common Pb (5.9%).

W120 (Ky)

Monazite grains in kyanite-grade sample W120 reside in all three petrographic locations (syn-D_1 garnet, matrix and post-D_1 garnet) and appear generally homogeneous, with no zoning visible with BSE imaging (Fig. 10d,e). Monazite inclusions in syn- and post-D_1 garnet are typically anhedral, whereas matrix monazite grains are typically subhedral and aligned within the S_1 foliation (Fig. 10d). Sample W120 has a single matrix population, with a lower intercept of 184.2 ± 1.5 Ma (Fig. 11b). Scatter in excess of analytical uncertainty is present when the single (older) monazite inclusion in syn-D_1 garnet is included with the matrix population. The three monazite grains from within post-D_1 garnet yield non-reproducible younger ages of *c.* 179–158 Ma.

W126 (Ky-Sil)

Monazite grains in kyanite- and sillimanite-bearing sample W126 are also found in all three petrographic settings and appear generally homogeneous in BSE (Fig. 10j). Monazite inclusions in syn- and post-D_1 garnet are typically anhedral, whereas matrix monazite grains are typically subhedral and aligned within the S_1 foliation. Sample W126 monazite data do not cluster into clear age populations (Fig. 11c). Older ages are preserved in syn-D_1 garnet (*c.* 193–184 Ma), overlapping and younger ages are preserved in the matrix (*c.* 191–169 Ma) and the youngest age is preserved in the post-D_1 garnet (*c.* 165 Ma).

W110 (Sil)

Monazite grains in sillimanite-grade sample W110 are located in syn-D_1 garnet and the matrix. The grains are typically homogeneous in BSE (Fig. 10n), with the exception of some inclusions in syn-D_1 garnet, which have bright, high-Th cores (Fig. 10b). Monazite inclusions in syn-D_1 garnet are typically anhedral, whereas matrix monazite grains are typically subhedral and aligned within the S_1 foliation (Fig. 10n). Sample W110 has a well-defined syn-D_1 garnet age (186.2 ± 1.8 Ma, $n = 5$) enveloped by a spread in matrix ages, between *c.* 192–173 Ma (Fig. 11d). These matrix ages form two groups at 188.0 ± 1.6 Ma and 179.4 ± 1.6 Ma. Analysis W110-8-5.1 was excluded from the syn-D_1 garnet regression as it contains high common Pb (7.4%), and analysis W110-13-1.1 was excluded as an outlier from the younger monazite population.

Interpretation

W122 (St)

As discussed above, staurolite-grade sample W122 was chosen as the lower bound for the present study, because it was the lowest-grade sample collected from the DSC that contained monazite (Table 1). Sample W122 is also notable for being the only sample that has a single monazite population, with the oldest intercept age of 191.5 ± 2.4 Ma (Fig. 11e). Given the similar chemistry between all of the samples, and the consistent allanite-monazite systematics (Table 1), initial monazite growth appears coincident with staurolite-grade *P–T* conditions for metapelites in the DSC. Therefore, the 191.5 ± 2.4 Ma intercept for sample W122 is interpreted to represent a near-peak age for this sample, and to define a staurolite-zone age for the DSC. The lack of monazite inclusions in garnet is also consistent with monazite growth at near-peak conditions after crystallization of most of the garnet.

By contrast, the three higher grade samples show variability in their monazite age populations to younger values. While many studies have shown the benefit of using monazite chemistry to interpret age variation (e.g. Foster *et al.*, 2000; Gibson *et al.*, 2004; Kohn *et al.*, 2005), such an approach seems better suited for distinguishing between sub- and supra-solidus monazite that has grown variably in the presence of garnet. Monazite from the DSC exhibits a weak correlation between older grains having a slightly higher Th content, but, in general, its chemistry is not clearly correlated with age (Table S1). Thus, we have focused on textural and contextual constraints to analyse the monazite results for the higher grade samples in this study.

W120 (Ky)

Kyanite-grade sample W120 has a single matrix age of 184.2 ± 1.5 Ma. This could be interpreted to approximate the age at which sample W120 experienced initial monazite growth, which, for the average DSC metapelite bulk rock chemistry, is argued above to correlate with reaching staurolite-grade *P–T* conditions (Table 1). However, a simple model of crustal

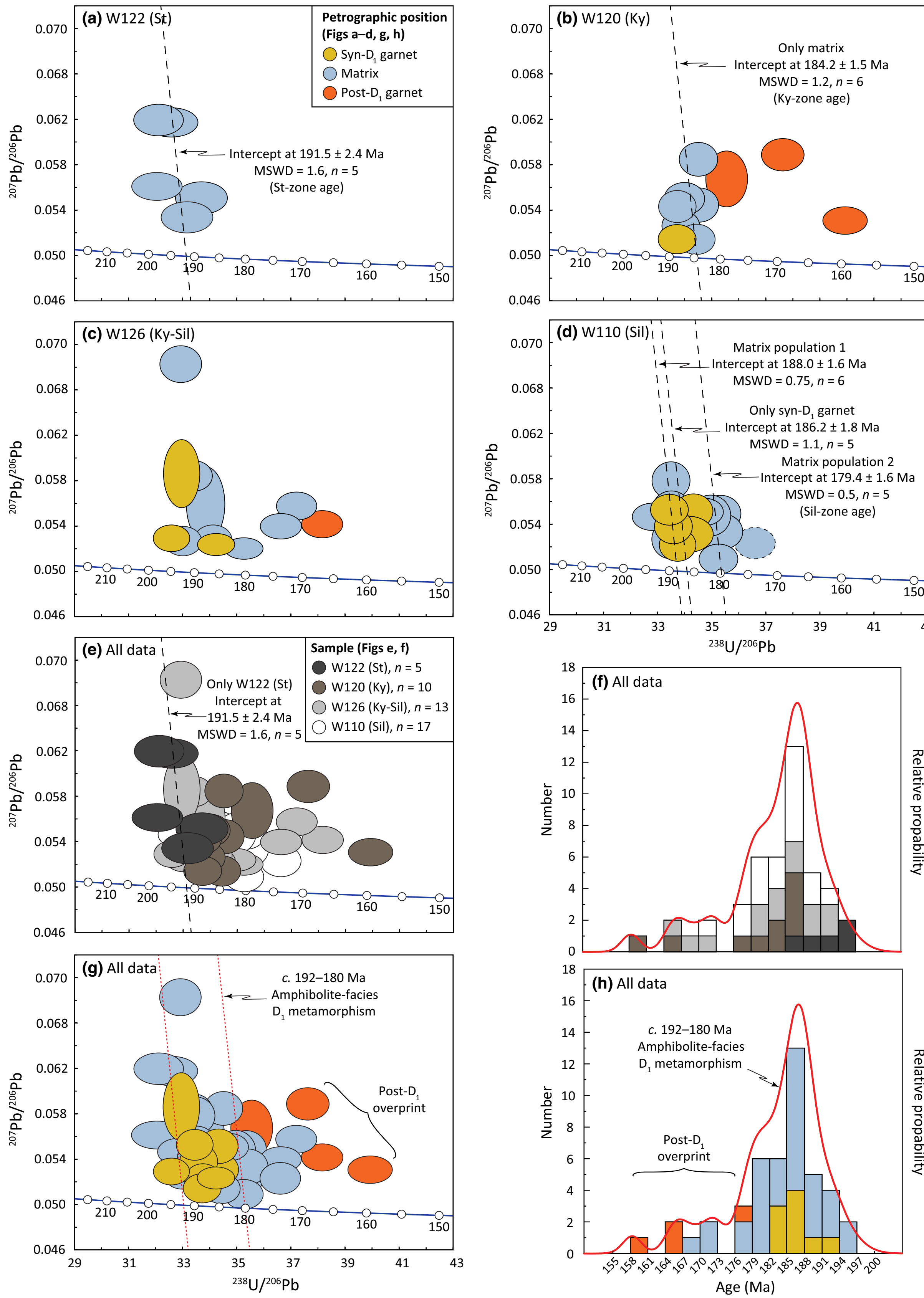
(a) W122 (St)
Petrographic position (Figs a–d, g, h)
Syn-D_1 garnet
Matrix
Post-D_1 garnet
Intercept at 191.5 ± 2.4 Ma
MSWD = 1.6, n = 5
(St-zone age)
(b) W120 (Ky)
Only matrix
Intercept at 184.2 ± 1.5 Ma
MSWD = 1.2, n = 6
(Ky-zone age)
(c) W126 (Ky-Sil)
(d) W110 (Sil)
Matrix population 1
Intercept at 188.0 ± 1.6 Ma
MSWD = 0.75, n = 6
Only syn-D_1 garnet
Intercept at 186.2 ± 1.8 Ma
MSWD = 1.1, n = 5
Matrix population 2
Intercept at 179.4 ± 1.6 Ma
MSWD = 0.5, n = 5
(Sil-zone age)
(e) All data
Only W122 (St)
Intercept at 191.5 ± 2.4 Ma
MSWD = 1.6, n = 5
Sample (Figs e, f)
W122 (St), n = 5
W120 (Ky), n = 10
W126 (Ky-Sil), n = 13
W110 (Sil), n = 17
(f) All data
(g) All data
c. 192–180 Ma
Amphibolite-facies
D_1 metamorphism
Post-D_1 overprint
(h) All data
c. 192–180 Ma
Amphibolite-facies
D_1 metamorphism
Post-D_1 overprint
$^{207}Pb/^{206}Pb$
$^{238}U/^{206}Pb$
Number
Relative propability
Age (Ma)

thickening predicts that higher grade samples would reach staurolite-grade P–T conditions before lower grade samples, which is inconsistent with the relative ages of W122 and W120. Instead, it is noted that the W120 matrix monazite are strongly aligned within the kyanite-bearing S_1-fabric (Fig. 10d), and it is suggested that the monazite experienced further growth and/or recrystallization with continued deformation into the kyanite zone. Therefore, the 184.2 ± 1.5 Ma is considered to represent a near-peak age for sample W120 and, by extension, a kyanite-zone age for the DSC. This could also explain the observation of the older age of the monazite inclusion in syn-D_1 garnet, which may be part of a slightly older population associated with initial monazite growth that has been reset in the matrix by subsequent reaction and/or deformation. The possible meanings of the young post-D_1 garnet ages are discussed below.

W110 (Sil)

Sillimanite-bearing sample W110 has two populations of matrix monazite: an older population (188.0 ± 1.6 Ma) that overlaps with the monazite inclusions in syn-D_1 garnet (186.2 ± 1.8 Ma), and a younger 179.4 ± 1.6 Ma group. Matrix monazite in this sample is notable for having multiple age domains (Fig. 10g), with no obvious chemical variations (Table S1). These observations suggest that matrix monazite experienced near-isochemical growth and/or recrystallization episodes. The younger domains are typically within the more faceted part of the grains, which align with S_1 (Fig. 10n). Continuing the logic from sample W120, the older matrix population and syn-D_1 garnet population are considered as part of an earlier phase of monazite growth on the prograde path, and the younger matrix monazite population (179.4 ± 1.6 Ma) is interpreted to reflect further growth and/or recrystallization of the monazite with continued deformation into the sillimanite zone. Consequently, the 179.4 ± 1.6 Ma age is interpreted to represent a near-peak age for this sample and, by extension, sillimanite-grade metamorphism in the DSC.

W126 (Ky-Sil)

A feature of this dataset is the reproducibility of the relative age ranges for the textural contexts within each sample, as suggested by the common signal that emerges in Fig. 11g,h of older syn-D_1 garnet ages, a spread in matrix ages and younger ages associated with the post-D_1 garnet. Therefore, although kyanite- and sillimanite-bearing sample W126 does not contain any clear populations (Fig. 11c), the sample appears to be consistent with overall dataset systematics.

Post-D_1 garnet inclusions

Figure 11h shows that the monazite data are primarily clustered from *c.* 194 to *c.* 179 Ma, below which a 'tail' of younger ages contains non-reproducible ages down to *c.* 158 Ma. Monazite inclusions within post-D_1 garnet are the dominant component of this young tail, and these ages are interpreted to represent post-peak monazite growth and/or crystallization in the DSC. Fluid flow is commonly cited as a driver of post-peak monazite recrystallization (e.g. Ayers *et al.*, 1999), and the extensive post-tectonic magmatism in the region provides a possible post-D_1 fluid source (Roger *et al.*, 2004). However, this is considered an unlikely mechanism, because the young ages are dominantly found in the post-D_1 garnet rather than the matrix, which might be expected to be more prone to late fluid flow and recrystallization. Several authors have noted a fundamental reaction coupling between garnet and monazite during metamorphism, with, for example, resorption of garnet being commonly associated with new monazite growth (Pyle & Spear, 2003). Therefore, it is suggested that the post-D_1 garnet monazite inclusions could represent the products of the partial resorption of the syn-D_1 garnet, with growth of the youngest monazite occurring in the immediate vicinity of the resorbing garnet (e.g. Gibson *et al.*, 2004). Monazite grains thus formed could then be trapped passively by subsequent post-D_1 garnet growth. In this scenario, the ages represent a maximum age for the post-D_1 garnet growth.

Summary

Integration of the results for staurolite-grade sample W122 (191.5 ± 2.4 Ma), kyanite-grade sample W120 (184.2 ± 1.5 Ma) and sillimanite-grade sample W110 (179.4 ± 1.6) suggests a 12 Ma period of thermal peak amphibolite facies conditions in the DSC. Over-

Fig. 11. Geochronology results. Tera-Wasserburg diagrams (TW) uncorrected for common Pb display error ellipses at the 2σ level. Regressions are anchored at a $^{207}Pb/^{206}$ ratio of 0.83 ± 0.02, which is a composition representing that acquired during mineral growth over the last *c.* 220 Ma (Stacey & Kramers, 1975). (a–d, g, h) are shaded by petrographic position and (e, f) are shaded by sample, with the legends shown in (a) and (e), respectively. (a) TW for sample W122 data. Regression for all data points. (b) TW for sample W120 data. Regression for monazite located in the matrix. (c) TW for sample W126 data. (d) TW for sample W110 data. Regressions for monazite located in syn-D_1 garnet and for two matrix populations. The dashed ellipse corresponds to a single data point that is excluded from the younger matrix population. (e) TW showing all data. Regression for monazite from sample W122. (f) Histogram with 3 Ma bins showing all data. (g) TW showing all data. (h) Histogram with 3 Ma bins showing all data.

all, the data are interpreted to be extremely consistent with the petrographic framework developed above, which predicts that Barrovian metamorphism in the DSC occurred predominantly during D_1 with some subtle post-D_1 overprinting.

DISCUSSION

Barrovian metamorphism in the DSC

Figure 2 shows a theoretical example of *P–T–t* paths for a suite of cogenetic samples involved in crustal thickening. Figure 12a shows an equivalent documentation of metamorphism in the DSC, and summarizes the main results of this study. Biotite- and melt-zone limits from Huang *et al.* (2003a) are included to extend the scope of this study, and help further define the metamorphic field gradient (Richardson & England, 1979; Thompson & England, 1984; Spear, 1993). Calculating a field gradient from an obliquely exposed crustal section requires a constancy of thermal and tectonic characteristics across the section being considered, in which case the gradient is a simple function of depth (Harte & Dempster, 1987). The observation that isograds occur at variable stratigraphic levels through the DSC (Fig. 1b) suggests that this is not an assumption that can be simply made for the DSC. Nevertheless, for the purposes of discussion, this assumption is initially made, prior to evaluating the simplification.

Several features of Fig. 12a coincide with those shown on Fig. 2: the partial *P–T* paths are nested and have a clockwise sense; higher grade samples reach peak conditions at sequentially younger ages; the array of peak conditions form a metamorphic field gradient concave to the *T*-axis; the field gradient is polychronic, with a 12 Ma duration of thermal peak amphibolite facies conditions; and the geotherms are transient. There are also some clear differences. Most notably, in Fig. 12a the *P–T* path segments and the field gradient have similar slopes and peak *P* and *T* coincide for samples W122 and W120. These differences stem from a fundamental assumption in the thermal models used to generate the curves in Fig. 2, namely that rapid burial is followed by erosion. Under such conditions, T_{max} is necessarily reached during decompression, due to the time lag of thermal relaxation. In contrast, if a given rock pile undergoes sustained slow burial, then thermal equilibrium is approached during compression, causing the *P–T* paths and the metamorphic field gradient to progressively merge (England & Thompson, 1984). Figure 12a is suggested to be more consistent with the latter scenario, implying that the DSC, and by extension the Songpan-Garzê Fold Belt, experienced slow tectonic burial, without extensive concomitant erosion.

Two geotherms are shown on Fig. 12a that bracket the *P–T* path segments for samples W122 and W120, which suggest that the geotherm evolved from 150 °C $kbar^{-1}$ ($\sim$40 °C km^{-1}) at the start of garnet growth in sample W122, to 100 °C $kbar^{-1}$ ($\sim$27 °C km^{-1}) at the end of garnet growth in sample W120 (Fig. 12). T_{max} positions for samples W126 and W110 suggest that an inflexion is reached around the kyanite-sillimanite transition, at which point the geotherm reaches a minimum (i.e. coldest) and starts to sweep to steeper gradients, as per Fig. 2. The melt-zone limits from Huang *et al.* (2003a) would continue this extrapolation back towards hotter gradients of $\sim$120 °C $kbar^{-1}$ ($\sim$32 °C km^{-1}). Beyond the inflexion point, *P–T* paths should start to approach T_{max} from slightly higher pressures. The effect of slow burial is to delay the point at which the samples decompress during heating, so that the recorded pressures of the Danba field gradient are close to P_{max}. This is in contrast with Fig. 2, whereby the metamorphic field gradient is not representative of the peak pressure reached by any given sample (England & Richardson, 1977).

Figure 12b considers the required trajectories of a metamorphic field gradient in developing a Barrovian sequence, using the pseudosection from sample W122 (Fig. 7c) as a template (because this pseudosection considers the largest *P–T* space). As the pseudosection reaction topology of pelitic bulk compositions is fairly consistent (Caddick & Thompson, 2008), this discussion is broadly generic to metapelites. The Barrovian isograds are highlighted and a low-pressure limit to Barrovian metamorphism is identified, below which no kyanite would be observed. This corresponds to the kyanite–sillimanite transition in the presence of staurolite, and is equivalent to the bathograd 4/5 boundary identified by Carmichael (1978). Above this limit, a wide range of broadly concave field gradients would generate Barrovian sequences. Carmichael (1978) split this range into two bathozones, using the intersection of the solidus and the kyanite–sillimanite transition as the boundary. However, White *et al.* (2001) noted that the wet solidus can produce fairly cryptic volumes of melt in metapelites, and suggested that reaching muscovite dehydration is the 'effective solidus'. Also, this study shows that variable a_{H_2O} can have a large effect on the pressure of this intersection. Therefore, an alternative demarcation is suggested. Based on the fairly constant nature of the rutile-ilmenite shelf in metapelitic systems under reducing conditions (White, 2000; Caddick & Thompson, 2008), rutile-present and rutile-absent could be considered a useful subdivision of Barrovian sequences into high- and low-pressure varieties. Under this scheme, the DSC is an example of low-pressure Barrovian metamorphism. The calculated Danba field gradient is in fact observed to traverse near the low-pressure limit of Barrovian metamorphism (Fig. 12b). This is consistent with the fact that the metamorphism was generated solely within a thickened cover sequence, as opposed to

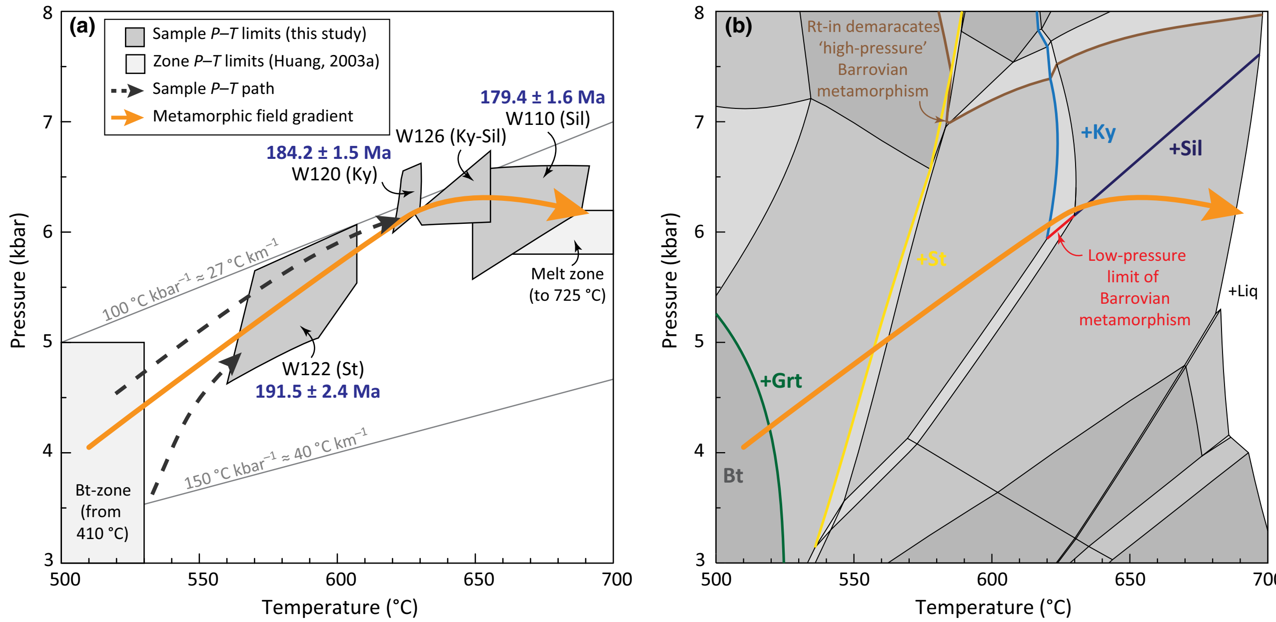

Fig. 12. Amalgamated results of this study. (a) In the style of Fig. 2, but quantified for the DSC. The *P–T* path segments and sample T_{max} limits are taken from Figs 7 & 8. Biotite- and melt-zone *P–T* limits are from Huang *et al.* (2003a) and extend the scope of this study. These estimates were calculated using the avPT function of THERMOCALC (Powell & Holland, 1994) at a similarly reduced a_{H_2O} to this study. The *t* constraints are shown in Fig. 11. Geotherms are drawn as a straight line that goes through the origin. Conversion from °C kbar^{-1} to °C km^{-1} assumes a crustal density of 2750 kg m^{-3}. The results suggest slow burial of the DSC during the early Jurassic, which caused a single, extended episode of relatively low-pressure, Barrovian-type metamorphism; see text for discussion. (b) The Danba metamorphic field gradient is overlain on the pseudosection shown in Fig. 7c for sample W120, with Barrovian isograds highlighted. The Danba field gradient is observed to lie at the low-pressure end of possible trajectories that would give a Barrovian sequence for this bulk composition; see text for discussion.

beneath an overthrusting continental plate, where higher pressure regional metamorphism would be induced (e.g. Searle *et al.*, 2006).

As stated above, the variations in the distribution of isograds in the DSC (e.g. no kyanite zone is observed on the eastern transect of the DSC; Fig. 1b) suggest some thermotectonic variation. This implies that no one field gradient could characterize the whole DSC. Nevertheless, the one shown on Fig. 12 is considered coarsely representative of the thermal structure of the DSC for two reasons. First, it is notable that the Danba field gradient lies close to the low-pressure limit of Barrovian metamorphism, below which no kyanite zone would be expected (Fig. 12b). Therefore, it would only take a slight increase in temperature or decrease in pressure to transition directly from staurolite- to sillimanite-bearing assemblages (as seen in the eastern DSC). Second, the relative consistency of the mapped mineral isograd sequence in the DSC (bar the one variation noted above) points to a relatively consistent thermal architecture at the regional scale. Nevertheless, this highlights the complexities of using natural case studies and it is likely that only the ideal condition of small geographical area and significant variation in structural relief is capable of revealing a single metamorphic field gradient for a given area (England & Richardson, 1977). Finally, it is clear that any given field gradient will only have a finite extent, as lateral variation in heat flow and age of metamorphism are features of many orogenic belts, and indeed are a feature of the type area for Barrovian metamorphism in the Scottish Highlands, which transitions to Buchan-style metamorphism to the northeast (Harte & Hudson, 1979).

Timing of sillimanite-grade metamorphism in the DSC

One objective of this study was to resolve whether the sillimanite-grade metamorphism in the DSC was continuous with the kyanite-grade metamorphism during formation of the Songpan-Garzê Fold Belt, or whether it represents a thermal overprint. The petrography, pseudosection modelling and geochronology presented strongly suggest that all high-grade metamorphism in the DSC was progressive with, and solely caused by, slow thickening of the Songpan-Garzê Fold Belt during the late Triassic to early Jurassic. This is evidenced by all index minerals aligning within S_1 fabrics, the T_{max} positions of all of the study samples defining a smooth array, and the sequential nature of the monazite ages.

Ambiguity surrounding metamorphism in the DSC primarily stems from conflicting published ages for the sillimanite-grade metamorphism (see Introduction). The monazite age data in this study are interpreted above to reflect sillimanite-grade conditions being reached at 179.4 ± 1.6 Ma, as part of a continuum of metamorphism from staurolite-grade conditions at 191.5 ± 2.4 Ma. No evidence was found in this study to support the *c.* 65 Ma age presented by Wallis *et al.* (2003), and it is unclear what event is recorded by this date. The high-temperature age data presented by Huang *et al.* (2003b) have a similar age range to this study of *c.* 200–160 Ma. However, the present study disagrees with the interpretations made by Huang *et al.* (2003b), which distinguished kyanite-grade metamorphism at *c.* 204–190 Ma and a sillimanite-grade thermal overprint at *c.* 168–158 Ma, for three reasons.

First, the interpretation of the data in Huang *et al.* (2003b) was partly based on their petrographic interpretation that sillimanite growth was part of a second fabric forming event (D_2; same orientation as this study) in the DSC. This observation is counter to many other studies, which observed that all Barrovian minerals were contained within D_1 fabrics (Mattauer *et al.*, 1992; Wallis *et al.*, 2003; Cheng & Lai, 2005). Furthermore, it seems at odds with their own observations, which detailed that D_2 folded the sillimanite-in isograd. The present study also notes that D_2 is associated with low-temperature microstructures and emphatically places sillimanite growth during D_1. Second, the U–Pb monazite data presented by Huang *et al.* (2003b) do not seem to support their conclusions as they recorded their youngest ages in a kyanite-grade sample, and their sillimanite-grade sample had ages of *c.* 197–180 Ma. Third, the conclusions made by Huang *et al.* (2003b) included results from U–Pb titanite and garnet Sm–Nd techniques together with the U–Pb monazite data. However, the former two techniques have closure temperatures below peak temperatures in the region (Mezger *et al.*, 1992; Scott & St-Onge, 1995), so are considered unsuitable for dating peak metamorphism, particularly in the context of the DSC where slow burial and exhumation are suggested to have sustained high temperatures. Instead, it is suggested that many of the observations made by Huang *et al.* (2003b) are more consistent with the notion of a progressive D_1 event, and the noted age dispersion is due to the combined effects of sustained high temperatures in the region, partial post-peak overprinting and real dispersion in ages reflecting resolvable timescales of prograde metamorphism.

Regional tectonic implications

The results of the present study seem applicable to the whole of the Songpan-Garzê Fold Belt, as similar low-pressure (5–7 kbar), kyanite-grade Barrovian metamorphism is reported from the Xuelongbao region of the central Longmen Shan mountains, with an age of 210–196 Ma (Dirks *et al.*, 1994; Worley *et al.*, 1997). Assuming a crustal density of 2750 kg m^{-3}, this suggests that the sedimentary pile reached up to ~26 km, indicating a doubling of thickness during formation of the Songpan-Garzê Fold Belt. Although it is unclear how thick the crust was prior to shortening, and how much shortening there was in the basement during inversion of the Songpan-Garze basin, clearly, the Songpan-Garzê Fold Belt was a region of thickened crust in the early Jurassic.

More broadly, the timing of crustal thickening and uplift of the plateau remains contentious (Clark, 2011). This study adds to the burgeoning evidence that Tibet experienced a widespread episode of crustal thickening during the late Triassic to early Jurassic (e.g. Yang *et al.*, 2009). This overlaps in time with the Indosinian orogeny, which is sporadically exposed in south-east Asia. Although the term Indosinian is *sensu stricto* only applicable to events within Vietnam (Carter & Clift, 2008), increasing numbers of Indosinian-epoch events are being documented in the wider region, suggesting that this was a major phase of continental accretion in Asia.

CONCLUSIONS

1 Petrographic, thermobarometric and geochronological results indicate that Barrovian metamorphism in the DSC was continuous and related to slow thickening of the Songpan-Garzê Fold Belt during the late Triassic to early Jurassic.
2 Fabrics in the DSC record a range of states in progressive cleavage development (S_1), associated with compression of the Songpan-Garzê Fold Belt (D_1). All index minerals align within or are wrapped by S_1, indicating that Barrovian metamorphism was developed during D_1. In the core of the DSC, an incipient crenulation cleavage (S_2) is developed that is associated with low-temperature microstructures (280–400 °C).
3 Calculated peak metamorphic conditions range from ~5.2 kbar and 580 °C at staurolite grade, to ~6.0 kbar and 670 °C at sillimanite grade, and effectively constrain a metamorphic field gradient. *P–T* path segments and the field gradient are approximately collinear. Slow burial concomitant with thermal relaxation is suggested to have collapsed the textbook schematic of broad, clockwise *P–T–t* loops that are typically associated with Barrovian metamorphism.
4 Monazite replaces allanite as the major REE-bearing mineral from staurolite grade onwards in the DSC. Given the similar bulk-rock chemistry between analysed samples, this suggests a link between initial monazite growth and staurolite-grade *P–T* conditions. Only the staurolite-grade sample rendered a single monazite population. All higher grade samples show evidence of multiple episodes of monazite growth and/or recrystallization. Staurolite-grade conditions were reached at 191.5 ± 2.4 Ma. Kyanite-grade conditions were attained at 184.2 ± 1.5 Ma. Sillimanite-grade con-

ditions continued until 179.4 ± 1.6 Ma. Overall, thermal peak amphibolite facies metamorphism in the DSC lasted at least 12 Ma.

5 Petrographically and chemically defined post-D_1 garnet growth is associated with young monazite inclusions that have ages of *c*. 180–160 Ma. The growth of these monazite is suggested to be coupled with partial resorption of garnet.

6 Pseudosection modelling shows that a_{H_2O} can be an important control on the spacing of Barrovian index mineral isograds and $X_{Fe^{3+}}$ can have a moderate effect on garnet stability. The presence or absence of rutile from a Barrovian suite is suggested to differentiate between high- and low-pressure Barrovian metamorphism, respectively. In this context, Barrovian metamorphism was low pressure in the DSC.

7 Eastern Tibet experienced a significant phase of crustal thickening in the late Triassic to early Jurassic that is temporally associated with widespread Indosinian-epoch events throughout Asia.

ACKNOWLEDGEMENTS

The authors acknowledge a Natural Environmental Research Council (NERC) postgraduate grant to OMW, reference number NE/I528485/1, with this work forming part of the PhD research for the first author. The following people are thanked: K. Cook (NTU) and T. Xibin (CEA) for their support in the field, P. England (Oxford) for discussion, J. Hyde (Oxford) for thin section preparation, T. Pestaj (GSC) for SHRIMP support and P. Hunt (GSC) for SEM support. MPS was funded by a NERC grant, whereas MSO's travel and research and OMW's SHRIMP work were funded by the Earth Sciences Sector, Natural Resources Canada. Thorough and constructive comments from R. Berman (GSC), D. Pattison (University of Calgary) and R. White (Johannes Gutenberg University Mainz) are gratefully acknowledged. This is Earth Sciences Sector contribution no. 20130067.

REFERENCES

Allaz, J., Maeder, X., Vannay, J.-C. & Steck A., 2005. Formation of aluminosilicate-bearing quartz veins in the Simano nappe (Central Alps): structural thermobarometric and oxygen isotope constraints. *Schweizerische Mineralogische und Petrographische Mitteilungen*, **85,** 191–214.

Ayers, J.C., Miller, C., Gorisch, B. & Milleman, J., 1999. Textural development of monazite during high-grade metamorphism: hydrothermal growth kinetics with implications for U, Th–Pb geochronology. *American Mineralogist*, **84,** 1766–1780.

Barrow, G., 1893. On an Intrusion of Muscovite-biotite Gneiss in the South-eastern Highlands of Scotland and its accompanying Metamorphism. *Quarterly Journal of the Geological Society*, **49,** 330–358.

Barrow, G., 1912. On the geology of lower dee-side and the southern highland border. *Proceedings of the Geologists Association*, **23,** 274–291.

Berman, R.G., Sanborn-Barrie, M., Stern, R.A. & Carson, C.J., 2005. Tectonometamorphism at ca. 2.35 and 1.85 Ga in the Rae domain western Churchill Province Nunavut Canada: insights from structural metamorphic and in situ geochronological analysis of the southwestern Committee Bay belt. *The Canadian Mineralogist*, **43,** 409–442.

Burchfiel, B.C., Zhiliang, C., Yupinc, L. & Royden, L.H., 1995. Tectonics of the Longmen Shan and adjacent regions Central China. *International Geology Review*, **37,** 661–735.

Caddick, M.J. & Thompson, A.B. 2008. Quantifying the tecto-no-metamorphic evolution of pelitic rocks from a wide range of tectonic settings: mineral compositions in equilibrium. *Contributions to Mineralogy and Petrology*, **156,** 177–195.

Carmichael, D.M., 1969. On the mechanism of prograde metamorphic reactions in quartz-bearing pelitic rocks. *Contributions to Mineralogy and Petrology*, **20,** 244–267.

Carmichael, D.M., 1978. Metamorphic bathozones and bathograds: a measure of the depth of post-metamorphic uplift and erosion on the regional scale. *American Journal of Science*, **278,** 769–797.

Carter, A. & Clift, P., 2008. Was the Indosinian orogeny a Triassic mountain building or a thermotectonic reactivation event? *Comptes Rendus Geosciences*, **340,** 83–93.

Cheng, S. & Lai, X., 2005. Medium-low pressure metamorphism and *P–T* paths in Danba domain Sichuan province of western China. *Acta Petrologica Sinica*, **21,** 819–828.

Cheng, S., Lai, X. & You, Z., 2009. P–T paths derived from garnet growth zoning in Danba domal metamorphic terrain Sichuan Province West China. *Journal of Earth Science*, **20,** 219–240.

Chernoff, C. & Carlson, W.D., 1997. Disequilibrium for Ca during growth of pelitic garnet. *Journal of Metamorphic Geology*, **15,** 421–438.

Chinner, G.A., 1960. Pelitic Gneisses with varying Ferrous/Ferric Ratios from Glen Cova Angus Scotland. *Journal of Petrology*, **1,** 178–217.

Clark, M.K., 2011. Early Tibetan Plateau uplift history eludes. *Geology*, **39,** 991–992.

Coggon, R. & Holland, T.J.B., 2002. Mixing properties of phengitic micas and revised garnet-phengite thermobarometers. *Journal of Metamorphic Geology*, **20,** 683–696.

Dewey, J., Shackleton, R., Chengfa, C. & Yiyin, S., 1988. The tectonic evolution of the Tibetan Plateau. *Philosophical Transactions of the Royal Society of London. Series A: Mathematical amd Physical Sciences*, **327,** 379–413.

Diener, J.F.A. & Powell, R., 2010. Influence of ferric iron on the stability of mineral assemblages. *Journal of Metamorphic Geology*, **28,** 599–613.

Dirks, P., Wilson, C.J.L., Chen, S., Luo, Z. & Liu, S., 1994. Tectonic evolution of the NE margin of the Tibetan Plateau; evidence from the central Longmen Mountains, Sichuan Province, China. *Journal of Southeast Asian Earth Sciences*, **9,** 181–192.

England, P.C. & Richardson, S.W., 1977. The influence of erosion upon the mineral facies of rocks from different metamorphic environments. *Journal of the Geological Society*, **134,** 201–213.

England, P.C. & Thompson, A.B., 1984. Pressure–temperature–time paths of regional metamorphism II. Their inference and interpretation using mineral assemblages in metamorphic rocks. *Journal of Petrology*, **25,** 929–955.

Foster, G., Kinny, P., Vance, D., Prince, C. & Harris, N.B.W., 2000. The significance of monazite U–Th–Pb age data in metamorphic assemblages; a combined study of monazite and garnet chronometry. *Earth and Planetary Science Letters*, **181,** 327–340.

Gerya, T.V. & Maresch, W.V., 2004. Metapelites of the Kanskiy Granulite Complex (Eastern Siberia): kinked *P–T* paths and geodynamic model. *Journal of Petrology*, **45,** 1393–1412.

Gibson, H.D., Carr, S., Brown, R. & Hamilton, M., 2004. Correlations between chemical and age domains in monazite, and metamorphic reactions involving major pelitic phases:

an integration of ID-TIMS and SHRIMP geochronology with Y–Th–U X-ray mapping. *Chemical Geology*, **211,** 237–260.
Harrowfield, M.J. & Wilson, C.J.L., 2005. Indosinian deformation of the Songpan Garzê Fold Belt, northeast Tibetan Plateau. *Journal of Structural Geology*, **27,** 101–117.
Harte, B. & Dempster, T.J., 1987. Regional metamorphic zones: tectonic controls. *Philosophical Transactions of the Royal Society A: Mathematical, Physical and Engineering Sciences*, **321,** 105–127.
Harte, B. & Hudson, N.F.C., 1979. Pelite facies series and the temperatures and pressures of Dalradian metamorphism in E Scotland. *Geological Society, London, Special Publications*, **8,** 323–337.
Henry, D.J., Guidotti, C.V. & Thomson, J.A., 2005. The Ti-saturation surface for low-to-medium pressure metapelitic biotites: implications for geothermometry and Ti-substitution mechanisms. *American Mineralogist*, **90,** 316–328.
Holland, T.J.B. & Powell, R., 1998. An internally consistent thermodynamic data set for phases of petrological interest. *Journal of Metamorphic Geology*, **16,** 309–343.
Holland, T.J.B. & Powell, R., 2003. Activity–composition relations for phases in petrological calculations: an asymmetric multicomponent formulation. *Contributions to Mineralogy and Petrology*, **145,** 492–501.
Hou, L.W., Fu, X.F., Li, R.Q. & Yang, X.J., 1996. China Geological Map, 1:50,000 Danba Sheet and Explanatory Note. Geological Publishing House, page 62.
Huang, M., Buick, I.S. & Hou, L.W., 2003a. Tectonometamorphic Evolution of the Eastern Tibet Plateau: evidence from the Central Songpan-Garzê Orogenic Belt, Western China. *Journal of Petrology*, **44,** 255–278.
Huang, M., Maas, R., Buick, I.S. & Williams, I.S., 2003b. Crustal response to continental collisions between the Tibet, Indian, South China and North China Blocks: geochronological constraints from the Songpan-Garzê Orogenic Belt, western China. *Journal of Metamorphic Geology*, **21,** 223–240.
Jamieson, R.A., Beaumont, C., Fullsack, P. & Lee, B., 1998. Barrovian regional metamorphism: where's the heat?. *Geological Society, London, Special Publications*, **138,** 23–51.
Janots, E., Brunet, F., Goffé, B., Poinssot, C., Burchard, M. & Cemič, L., 2007. Thermochemistry of monazite-(La) and dissakisite-(La): implications for monazite and allanite stability in metapelites. *Contributions to Mineralogy and Petrology*, **154,** 1–14.
Janots, E., Engi, M., Berger, A., Allaz, J., Schwarz, J.-O. & Spandler, C., 2008. Prograde metamorphic sequence of REE minerals in pelitic rocks of the Central Alps: implications for allanite-monazite-xenotime phase relations from 250 to 610 °C. *Journal of Metamorphic Geology*, **26,** 509–526.
Kirby, E., Reiners, P.W., Krol, M.A., Whipple, K.X. *et al.*, 2002. Late Cenozoic evolution of the eastern margin of the Tibetan Plateau: inferences from $^{40}Ar/^{39}Ar$ and (U–Th)/He thermochronology. *Tectonics*, **21,** 1–20.
Kohn, M.J. & Malloy, M.A., 2004. Formation of monazite via prograde metamorphic reactions among common silicates: implications for age determinations. *Geochimica*, **68,** 101–113.
Kohn, M.J. & Spear, F.S., 2000. Retrograde net transfer reaction insurance for pressure-temperature estimates. *Geology*, **28,** 1127–1130.
Kohn, M.J., Wieland, M., Parkinson, C. & Upreti, B., 2005. Five generations of monazite in Langtang gneisses: implications for chronology of the Himalayan metamorphic core. *Journal of Metamorphic Geology*, **23,** 399–406.
Ludwig, K., 2003. User's Manual for Isoplot/Ex rev. 3.00: a Geochronological Toolkit for Microsoft Excel. Special Publications, 4, Berkeley Geochronology Center, Berkeley. Technical report.
Mahar, E., Baker, J., Powell, R., Holland, T.J.B. & Howell, N., 1997. The effect of Mn on mineral stability in metapelites. *Journal of Metamorphic Geology*, **15,** 223–238.
Mattauer, M., Malavieille, J., Calassou, S., Lancelot, J. *et al.*, 1992. La chaine Triasique de Songpan-Garzê (Ouest Sechuan at Est Tibet): une chaine de plissement-decollement sur marge passive. *Comptes Rendues de L'Academie des Sciences. Serie II*, **314,** 619–626.
Mezger, K., Essene, E.J. & Halliday, A.N., 1992. Closure temperatures of the Sm–Nd system in metamorphic garnets. *Earth and Planetary Science Letters*, **113,** 397–409.
Ohmoto, H. & Kerrick, D., 1977. Devolatilization equilibria in graphitic systems. *American Journal of Science*, **277,** 1013–1044.
Passchier, C.W. & Trouw, R.A.J., 2005. *Microtectonics*, 2nd edn. Springer.
Powell, R. & Holland, T.J.B., 1994. Optimal geothermometry and geobarometry. *American Mineralogist*, **79,** 120–133.
Powell, R. & Holland, T.J.B., 2008. On thermobarometry. *Journal of Metamorphic Geology*, **26,** 155–179.
Powell, R., Holland, T.J.B. & Worley, B., 1998. Calculating phase diagrams involving solid solutions via non-linear equations, with examples using THERMOCALC. *Journal of Metamorphic Geology*, **16,** 577–588.
Pyle, J.M. & Spear, F.S., 2003. Four generations of accessory-phase growth in low-pressure migmatites from SW New Hampshire. *American Mineralogist*, **88,** 338–351.
Rayner, N. & Stern, R.A., 2002. Improved sample preparation method for SHRIMP analysis of delicate mineral grains exposed in thin sections. Geological Survey of Canada, Current Research 2002-F10.
Richardson, S.W. & England, P.C., 1979. Metamorphic consequences of crustal eclogite production in overthrust orogenic zones. *Earth and Planetary Science Letters*, **42,** 183–190.
Roger, F., Calassou, S., Lancelot, S., Malavieille, J. *et al.*, 1995. Miocene emplacement and deformation of the Konga Shan granite (Xianshui He fault zone, west Sichuan, China): geodynamic implications. *Earth and Planetary Science Letters*, **130,** 201–216.
Roger, F., Malavieille, J., Leloup, P.H., Calassou, S. & Xu, Z., 2004. Timing of granite emplacement and cooling in the Songpan-Garzê Fold Belt (eastern Tibetan Plateau) with tectonic implications. *Journal of Asian Earth Sciences*, **22,** 465–481.
Roger, F., Jolivet, M. & Malavieille, J., 2008. Tectonic evolution of the Triassic fold belts of Tibet. *Comptes Rendus Geosciences*, **340,** 180–189.
Roger, F., Jolivet, M. & Malavieille, J., 2010. The tectonic evolution of the Songpan-Garzê (North Tibet) and adjacent areas from Proterozoic to Present: a synthesis. *Journal of Asian Earth Sciences*, **39,** 254–269.
Schärer, U., 1984. The effect of initial ^{230}Th disequilibrium on young U–Pb ages: the Makalu case, Himalaya. *Earth and Planetary Science Letters*, **67,** 191–204.
Scott, D.J. & St-Onge, M.R., 1995. Constraints on Pb closure temperature in titanite based on rocks from the Ungava orogen, Canada: implications for U–Pb geochronology and P–T–t path determinations. *Geology*, **23,** 1123–1126.
Searle, M.P., Law, R.D. & Jessup, M., 2006. Crustal structure, restoration and evolution of the Greater Himalaya in Nepal-South Tibet: implications for channel flow and ductile extrusion of the middle crust. *Geological Society, London, Special Publications*, **268,** 355–378.
Smith, H.A. & Barreiro, B., 1990. Monazite U–Pb dating of staurolite grade metamorphism in pelitic schists. *Contributions to Mineralogy and Petrology*, **105,** 602–615.
Spear, F.S., 1993. *Metamorphic Phase Equilibria and Pressure-Temperature-Time Paths*. Mineralogical Society of America, Monograph Series, Washington, D.C.
Spear, F.S., 2010. Monazite-allanite phase relations in metapelites. *Chemical Geology*, **279,** 55–62.
Stacey, J.S. & Kramers, J.D., 1975. Approximation of terrestrial lead isotope evolution by a two-stage model. *Earth and Planetary Science Letters*, **26,** 207–221.
Stern, R.A. & Berman, R.G., 2000. Monazite U–Pb and Th–Pb geochronology by ion microprobe, with an application to

in situ dating of an Archean metasedimentary rock. *Chemical Geology*, **172,** 113–130.
Stipp, M., Stunitz, H., Heilbronner, R. & Schmid, S.M., 2002. The eastern Tonale fault zone: a 'natural laboratory' for crystal plastic deformation of quartz over a temperature range from 250 to 700 °C. *Journal of Structural Geology*, **24,** 1861–1884.
Thompson, A.B. & England, P.C., 1984. Pressure–Temperature–Time Paths of Regional Metamorphism II. Their Inference and Interpretation using Mineral Assemblages in Metamorphic Rocks. *Journal of Petrology*, **25,** 929–955.
Tinkham, D.K., Zuluaga, C. & Stowell, H., 2001. Metapelite phase equilibria modeling in MnNCKFMASH: the effect of variable Al_2O_3 and MgO/(MgO+FeO) on mineral stability. *Geological Materials Research*, **3,** 1–42.
Tracy, R.J., 1982. Compositional zoning and inclusions in metamorphic minerals. *Reviews in Mineralogy*, **10,** 762–775.
Tung, Y., Tan, X., Lee, Y., Cook, K. & Xu, X., 2011. Cenozoic Exhumation History of the Danba Domal Metamorphic Terrane, Eastern Songpan-Ganza Orogenic Belt, Western China. In American Geophysical Union, Fall Meeting 2011, abstract #T13F-2472.
Wallis, S., Tsujimori, T., Aoya, M., Kawakami, T. *et al*., 2003. Cenozoic and Mesozoic metamorphism in the Longmenshan orogen: implications for geodynamic models of eastern Tibet. *Geology*, **31,** 745.
Wang, K.-L., 2004. Geochemical constraints for the genesis of post-collisional magmatism and the geodynamic evolution of the Northern Taiwan region. *Journal of Petrology*, **45,** 975–1011.
Waters, D.J. & Lovegrove, D.P., 2002. Assessing the extent of disequilibrium and overstepping of prograde metamorphic reactions in metapelites from the Bushveld Complex aureole, South Africa. *Journal of Metamorphic Geology*, **20,** 135–149.
White, R.W., 2000. The effect of TiO_2 and Fe_2O_3 on metapelitic assemblages at greenschist and amphibolite facies conditions: mineral equilibria calculations in the system K_2O-FeO-MgO-Al_2O_3-SiO_2-H_2O-TiO_2-Fe_2O_3. *Journal of Metamorphic Geology*, **18,** 497–511.
White, R.W., Powell, R. & Holland, T.J.B., 2001. Calculation of partial melting equilibria in the system Na_2O-CaO-K_2O-FeO-MgO-Al_2O_3-SiO_2-H_2O (NCKFMASH). *Journal of Metamorphic Geology*, **19,** 139–153.
White, R.W., Pomroy, N.E. & Powell, R., 2005. An in situ metatexite-diatexite transition in upper amphibolite facies rocks from Broken Hill, Australia. *Journal of Metamorphic Geology*, **23,** 579–602.
White, R.W., Powell, R. & Holland, T.J.B., 2007. Progress relating to calculation of partial melting equilibria for metapelites. *Journal of Metamorphic Geology*, **25,** 511–527.
Whitney, D.L. & Evans, B.W., 2010. Abbreviations for names of rock-forming minerals. *American Mineralogist*, **95,** 185–187.
Wing, B.A., Ferry, J.M. & Harrison, T.M., 2003. Prograde destruction and formation of monazite and allanite during contact and regional metamorphism of pelites: petrology and geochronology. *Contributions to Mineralogy and Petrology*, **145,** 228–250.
Woodsworth, G.J., 1977. Homogenization of zoned garnets from pelitic schists. *Canadian Mineralogist*, **15,** 230–242.
Worley, B., Powell, R. & Wilson, C.J.L., 1997. Crenulation cleavage formation: evolving diffusion, deformation and equilibration mechanisms with increasing metamorphic grade. *Journal of Structural Geology*, **19,** 1121–1135.
Xu, G. & Kamp, P.J.J., 2000. Tectonics and denudation adjacent to the Xianshuihe Fault, eastern Tibetan Plateau: constraints from fission track thermochronology. *Journal of Geophysical Research*, **105,** 231–251.
Xu, X., Wen, X., Yu, G., Chen, G. *et al*., 2009. Coseismic reverse- and oblique-slip surface faulting generated by the 2008 Mw 7.9 Wenchuan earthquake, China. *Geology*, **37,** 515–518.
Yang, J., Xu, Z., Li, Z., Xu, X. *et al*., 2009. Discovery of an eclogite belt in the Lhasa block, Tibet: a new border for Paleo-Tethys? *Journal of Asian Earth Sciences*, **34,** 76–89.
Zhou, M.-F., Yan, D.-P., Kennedy, A.K., Li, Y. & Ding, J., 2002. SHRIMP U-Pb zircon geochronological and geochemical evidence for Neoproterozoic arc-magmatism along the western margin of the Yangtze Block, South China. *Earth and Planetary Science Letters*, **196,** 51–67.

SUPPORTING INFORMATION

Additional Supporting Information may be found in the online version of this article at the publisher's web site:

Table S1. Monazite compositions at each of the SHRIMP analysis locations. Totals are normalized to 100% to assist comparison between grains.

Received 19 March 2013; revision accepted 7 August 2013.